

# Gas and Cosmic-Ray Properties in the MBM 53, 54, and 55 Molecular Clouds and the Pegasus Loop as Revealed by HI Line Profiles, Dust, and Gamma-Ray Data

T. MIZUNO,<sup>1</sup> K. HAYASHI,<sup>2</sup> J. METZGER,<sup>3</sup> I. V. MOSKALENKO,<sup>4</sup> E. ORLANDO,<sup>4,5,6</sup> A. W. STRONG,<sup>7</sup> AND H. YAMAMOTO<sup>8</sup>

<sup>1</sup>*Hiroshima Astrophysical Science Center, Hiroshima University, Higashi-Hiroshima, Hiroshima 739-8526, Japan*

<sup>2</sup>*Institute of Space and Astronautical Science, Japan Aerospace Exploration Agency, 3-1-1 Yoshinodai, Chuo-ku, Sagami-hara, Kanagawa 252-5210, Japan*

<sup>3</sup>*Department of Physics, The University of Chicago, Chicago, Illinois 60637, USA*

<sup>4</sup>*W. W. Hansen Experimental Physics Laboratory, Kavli Institute for Particle Astrophysics and Cosmology, Stanford University, Stanford, CA 94305, USA*

<sup>5</sup>*Department of Physics, University of Trieste and INFN, I-34127 Trieste, Italy*

<sup>6</sup>*Eureka Scientific, Oakland, CA 94602-3017, USA*

<sup>7</sup>*Max-Planck Institut für extraterrestrische Physik, D-85748 Garching, Germany*

<sup>8</sup>*Department of Physics and Astrophysics, Nagoya University, Chikusa-ku Nagoya 464-8602, Japan*

## ABSTRACT

In studying the interstellar medium (ISM) and Galactic cosmic rays (CRs), uncertainty of the interstellar gas density has always been an issue. To overcome this difficulty, we used a component decomposition of the 21-cm HI line emission and used the resulting gas maps in an analysis of  $\gamma$ -ray data obtained by the *Fermi* Large Area Telescope (LAT) for the MBM 53, 54, and 55 molecular clouds and the Pegasus loop. We decomposed the ISM gas into intermediate-velocity clouds, narrow-line and optically thick HI, broad-line and optically thin HI, CO-bright H<sub>2</sub>, and CO-dark H<sub>2</sub> using detailed correlations with the HI line profiles from the HI4PI survey, the *Planck* dust-emission model, and the *Fermi*-LAT  $\gamma$ -ray data. We found the fractions of optical depth correction to the HI column density and CO-dark H<sub>2</sub> to be nearly equal. We fitted the CR spectra directly measured at/near the Earth and the measured  $\gamma$ -ray emissivity spectrum simultaneously. We obtained a spectral break in the interstellar proton spectrum at  $\sim 7$  GeV, and found the  $\gamma$ -ray emissivity normalization agrees with the AMS-02 proton spectrum within 10%, relaxing the tension with the CR spectra previously claimed.

*Keywords:* Cosmic rays (329) — Gamma-rays (637) — Interstellar medium (847)

## 1. INTRODUCTION

Interstellar space in the Milky Way is permeated with ordinary matter (gas or dust), which is known as the interstellar medium (ISM). It also contains high-energy charged particles known as cosmic rays (CRs), an interstellar radiation field (ISRF), and a magnetic field. These components are mutually interacting, and they play important roles in many physical and chemical processes (e.g., star formation). Hence, they have been studied in various wavebands from radio to  $\gamma$ -rays (for a review, see, e.g., [Ferriere 2001](#)).

Cosmic  $\gamma$ -ray emission (with photon energies  $E \gtrsim 100$  MeV) is known to be a powerful probe for studying the ISM and Galactic CRs. High-energy CR protons and electrons interact with the interstellar gas or the ISRF and produce  $\gamma$ -rays through nucleon–nucleon interactions, electron bremsstrahlung, and inverse-Compton (IC) scattering. Because the ISM is essentially transparent to those  $\gamma$ -rays (e.g., [Moskalenko et al. 2006](#)), we can study the ISM distribution via  $\gamma$ -ray observations. Because the  $\gamma$ -ray production cross-section is independent of the chemical or thermodynamic state of the interstellar gas, cosmic  $\gamma$ -rays have been recognized as a unique tracer of the total column density of gas, regardless of its atomic or molecular state. If observations in other wavebands can be used to estimate the gas column density accurately, the CR spectrum and intensity distribution can be examined as well.

Usually, the distribution of neutral atomic hydrogen (HI) is measured directly via 21-cm line surveys (e.g., Dickey & Lockman 1990; Kalberla & Kerp 2009), assuming the optically thin approximation, and the distribution of molecular hydrogen ( $\text{H}_2$ ) is estimated indirectly from carbon monoxide (CO) line-emission surveys (e.g., Dame et al. 2001), assuming a linear conversion factor. However, some fraction of the ISM gas in optically thick HI or CO-dark  $\text{H}_2$  phases may be missed by these line surveys. Such “dark gas” can be studied using total gas tracers such as dust extinction, reddening, and emission (e.g., Reach et al. 1994) and  $\gamma$ -rays (e.g., Grenier et al. 2005). The work by Grenier et al. (2005) has been confirmed and improved by subsequent observations with the *Fermi* Large Area Telescope (LAT; Atwood et al. 2009). In addition, the *Planck* mission has provided an all-sky model of thermal emission from dust (Planck Collaboration XIX 2011; Planck Collaboration XI 2014) that is useful for the study of the ISM gas distribution because of its sensitivity and high angular resolution.

Despite these efforts, uncertainties in the ISM gas column density and the CR intensity are still uncomfortably large, by as much as a factor of  $\sim 50\%$  even in local environment (see, e.g., Grenier et al. 2015). This is mainly due to the uncertainty in the spin temperature ( $T_s$ ) of the HI gas, which affects the conversion from the 21-cm line intensity to the HI gas column density. To cope with this difficulty, some authors (e.g., Mizuno et al. 2016; Hayashi et al. 2019) have proposed to treat areas with high dust temperatures as optically thin HI and have used this assumption in analyzing *Fermi*-LAT  $\gamma$ -ray data. However, their method cannot distinguish gas phases along the line of sight, and hence, it is not applicable to the Galactic plane. Also, the composition of the dark gas (i.e., the fractions of the optically thick HI and CO-dark  $\text{H}_2$ ) is quite uncertain and is controversial. For example, while Fukui et al. (2015) proposed that optically thick HI dominates dark gas, Murray et al. (2018) claimed that dark gas is mainly molecular. Again, this is because the value of  $T_s$  is usually unknown, and neither dust nor  $\gamma$ -rays can distinguish between atomic and molecular gas phases.

HI absorption features (optical depth profile) are often well represented by Gaussians, supporting that gas motions within HI clouds have a random velocity distribution. HI emission profiles of most sources can also be decomposed into Gaussians, and components with narrow or broad linewidths could be assumed to mainly arise from the cold neutral medium (CNM) or warm neutral medium (WNM), respectively (e.g., Kalberla et al. 2020). Recently, Kalberla & Haud (2018) analyzed the all-sky HI4PI survey data (HI4PI Collaboration 2016) and decomposed the HI 21-cm line emission into Gaussian lines by taking account of spatial coherence. Although their study uses emission spectra only and hence suffers from systematic uncertainties in separating the CNM and WNM, it allows them to study HI line profiles over the entire sky. Subsequently, Kalberla et al. (2020) found that narrow-line HI gas is associated with the dark gas estimated from infrared dust-emission maps by Schlegel et al. (1998). Specifically, HI lines with Doppler temperature  $T_D \leq 1000$  K (defined as  $22 \times \delta_v^2$  where  $\delta_v$  is the Gaussian linewidth in  $\text{km s}^{-1}$ ) are associated with gas for which the column density is significantly larger than the optically thin case. Their work opens the possibility of identifying optically thin HI and “dark gas” using HI line profile information and hence of decomposing the gas phases along the line of sight. We note that Kalberla et al. (2020) used HI emission data only to decompose narrow-line HI gas and attributed it to the dark gas, hence their results should be validated by an independent way. We also note that, although they interpreted the dark gas to be primarily CO-dark  $\text{H}_2$ , the thick HI hypothesis was not ruled out. To validate their work and establish a method applicable to the Galactic plane, we employed an HI-line-profile-based analysis to the MBM 53, 54, and 55 clouds and the Pegasus loop. They are nearby (100–150 pc) high-latitude clouds (Welty et al. 1989; Yamamoto et al. 2006) and hence are suitable for the detailed study of the ISM gas and CRs in the local environment. This region has been previously studied by Mizuno et al. (2016) using HI, dust, and  $\gamma$ -ray data but with a different method. Specifically, since Mizuno et al. (2016) modeled  $\gamma$ -ray data using dust maps as a tracer of the total gas column density, they cannot distinguish optically thick HI and CO-dark  $\text{H}_2$ . Also, the gas-to-dust ratio was calibrated using a small area with high dust temperature, and hence has large uncertainty. We aim to overcome these difficulties by using HI linewidth information in this study.

This paper is organized as follows. We describe the properties of the ISM gas templates in Section 2, and the  $\gamma$ -ray observations, data selection, and modeling in Section 3. The results of the data analysis are presented in Section 4, where we confirm that narrow HI traces dark gas. We also find there remain residuals and employ a dust map to trace this residual gas. We interpret narrow HI and residual gas template trace different phases of dark gas, and discuss the ISM properties in Section 5. We also compare obtained  $\gamma$ -ray emissivity and CR spectra measured at/near the Earth and discuss CR properties in Section 5. Finally, a summary of the study and future prospects are presented in Section 6.

## 2. ISM GAS TEMPLATES AND THEIR PROPERTIES

We analyzed the  $\gamma$ -ray data in the region of Galactic longitude  $60^\circ \leq l \leq 120^\circ$  and Galactic latitude  $-60^\circ \leq b \leq -28^\circ$ , which encompasses the MBM 53, 54, and 55 cloud complexes and the Pegasus loop. We prepared templates of the ISM gas for the  $\gamma$ -ray data analysis, as we did in Mizuno et al. (2016), but with updates, particularly for the atomic-gas phase. Specifically, we prepared the following gas templates. All gas maps are stored in a HEALPix (Górski et al. 2005) equal-area sky map of order 9<sup>1</sup> with a mean distance of adjacent pixels of 6'9 (0.114 deg) and pixel size of 0.013 deg<sup>2</sup>.

### $W_{\text{HI}}$ maps divided by HI line widths:

We downloaded HI line profile fits by Kalberla et al. (2020)<sup>2</sup> for our region of interest (ROI) and for peripheral regions ( $\leq 5^\circ$  from the boundaries). They modeled HI 21-cm emission of the HI4PI survey data (with an angular resolution of 16'2 in full width at the half maximum (FWHM)) in each sky direction using several Gaussians. And they gave the normalization, center, and width of each Gaussian component. As described in Kalberla & Haud (2018), they required the residuals to be consistent with the noise level, and also required the number of the used Gaussians as low as possible by considering the information about the neighboring pixels. Negative normalizations or widths are given to suspicious lines (weak lines likely being artifacts due to the noise), and we discarded them in preparing the map. We then divided the HI data into three components: intermediate-velocity clouds (IVCs) (e.g., Wakker 2001), with velocities outside the range from  $-30$  to  $+20$  km s<sup>-1</sup> (Fukui et al. 2014; Mizuno et al. 2016); HI clouds with narrow linewidths ( $T_{\text{D}} \leq 1000$  K. See Kalberla et al. (2020). Hereafter, we call them “narrow HI”.); and those with broad linewidths ( $T_{\text{D}} \geq 1000$  K; hereafter called “broad HI”). The  $W_{\text{HI}}$  maps (maps of the integrated HI 21-cm line intensity) of these clouds are shown in Figure 1. Using the HI line profiles in map preparation is a major update over the work by Mizuno et al. (2016). In the narrow HI template, we can recognize coherent structures at around  $l = 84^\circ$  to  $96^\circ$  and  $b = -44^\circ$  to  $-30^\circ$  and an area of  $\sim 20^\circ \times 20^\circ$  around  $(l, b) \sim (109^\circ, -45^\circ)$ . These features correspond to the MBM 53-55 clouds and the Pegasus loop, respectively.

### $W_{\text{CO}}$ map:

As we did in Mizuno et al. (2016), we used a  $W_{\text{CO}}$  map (map of the integrated <sup>12</sup>CO (J=1–0) 2.6-mm line intensity) internally available to the LAT team. It combines the work by Dame et al. (2001) and new data at high Galactic latitudes. Those data were taken by two 1.2 m telescopes (one in the northern hemisphere and the other in the southern hemisphere) and smoothed to give an angular resolution of 18' (FWHM) and sampled in 0°:25 intervals. The new CO data include most of the high-latitude CO clouds in the region studied here. As described in Dame (2011), the CO spectra are filtered and integrated over velocities to suppress noise. This map also is shown in Figure 1.

### Planck dust-model maps:

Dust is a known tracer of the total gas column density, and it has been used to construct the dark-gas template for  $\gamma$ -ray data analysis (e.g., Abdo et al. 2010; Ackermann et al. 2011, 2012b). As we did in Mizuno et al. (2016), we used the Planck dust maps (of the radiance  $R$ , the opacity  $\tau_{353}$  at 353 GHz, and the dust temperature  $T_{\text{d}}$ ) of the public Data Release 1 (version R1.20)<sup>3</sup> described by the Planck Collaboration XI (2014). As reported in Mizuno et al. (2016), several areas have high  $T_{\text{d}}$ , indicating localized heating by stars. To reduce their effects on the  $\gamma$ -ray data analysis, we refilled these areas (in the  $R$ ,  $\tau_{353}$ , and  $T_{\text{d}}$  maps) with the average of the peripheral pixels; see Appendix A for details. We also newly employed dust maps of the Planck public Data Release 2 (version R2.00)<sup>4</sup> for comparison. We found that they are less affected by infrared sources, and we had to mask only one source using the same procedure. Both Data Release 1 and 2 maps have an angular resolution of 5' (FWHM).

The  $R$  and  $T_{\text{d}}$  maps from Planck Data Release 1 are shown in Figure 2. We can recognize the MBM 53-55 clouds and the Pegasus loop in the  $R$  map. The  $\tau_{353}$  map from Planck Data Release 1, and the  $R$  and  $\tau_{353}$  maps from

<sup>1</sup> This corresponds to the total number of pixels of  $12 \times (2^9)^2 = 3145728$ . (9 comes from the resolution index.)

<sup>2</sup> [https://www.astro.uni-bonn.de/hisurvey/AllSky\\_gauss/](https://www.astro.uni-bonn.de/hisurvey/AllSky_gauss/)

<sup>3</sup> [https://irsa.ipac.caltech.edu/data/Planck/release\\_1/all-sky-maps/](https://irsa.ipac.caltech.edu/data/Planck/release_1/all-sky-maps/)

<sup>4</sup> [https://irsa.ipac.caltech.edu/data/Planck/release\\_2/all-sky-maps/](https://irsa.ipac.caltech.edu/data/Planck/release_2/all-sky-maps/)

the *Planck* Data Release 2 exhibit similar but different contrasts, and they predict different total gas column density distributions. We test them against the  $\gamma$ -ray data in Section 4.1.

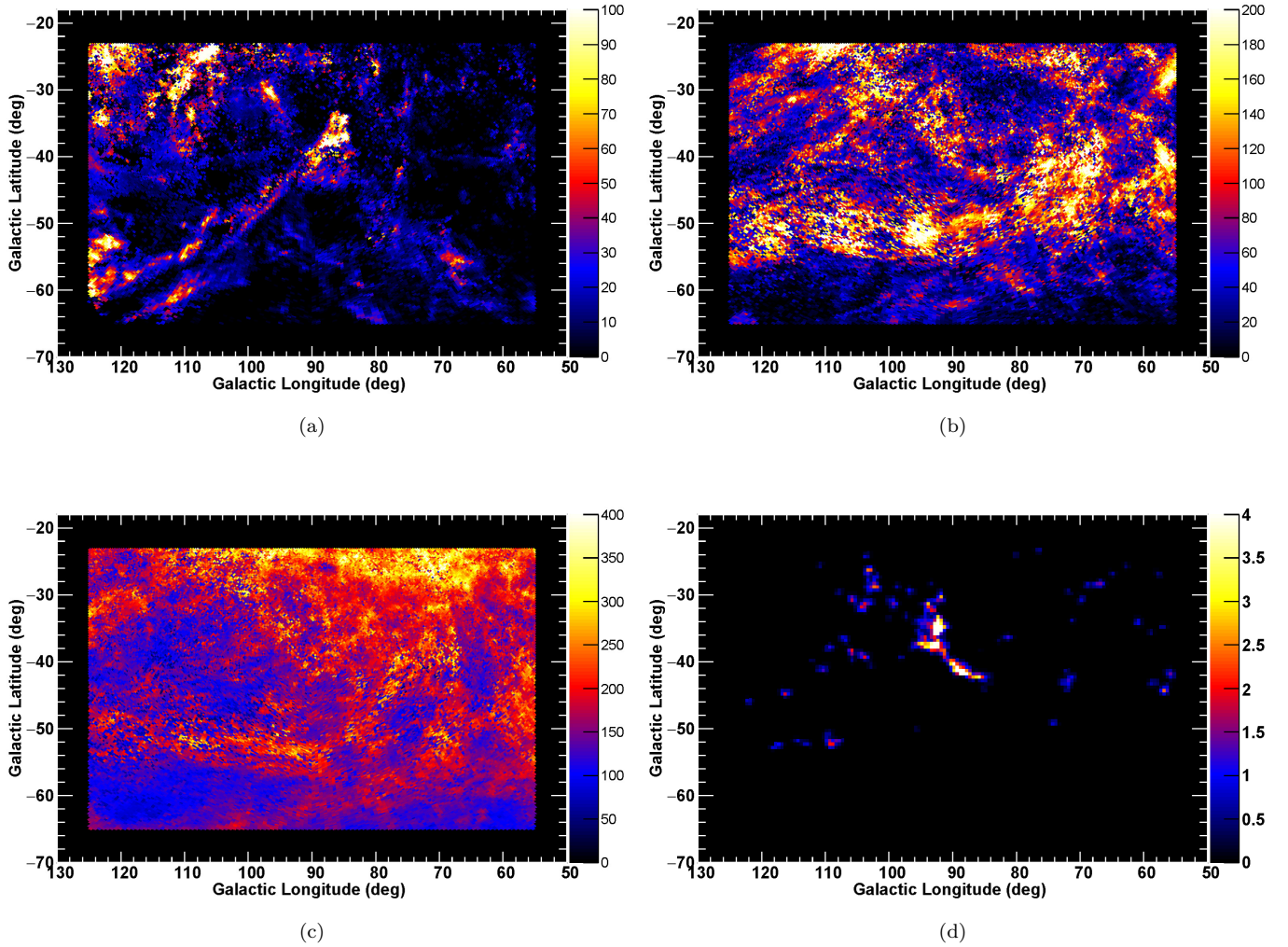


**Figure 1.** (a) The  $W_{\text{HI}}$  map of the IVCs; (b) the  $W_{\text{HI}}$  map of narrow HI; (c) the  $W_{\text{HI}}$  map of broad HI; and (d) the  $W_{\text{CO}}$  map. All these maps are shown in unit of  $\text{K km s}^{-1}$ .

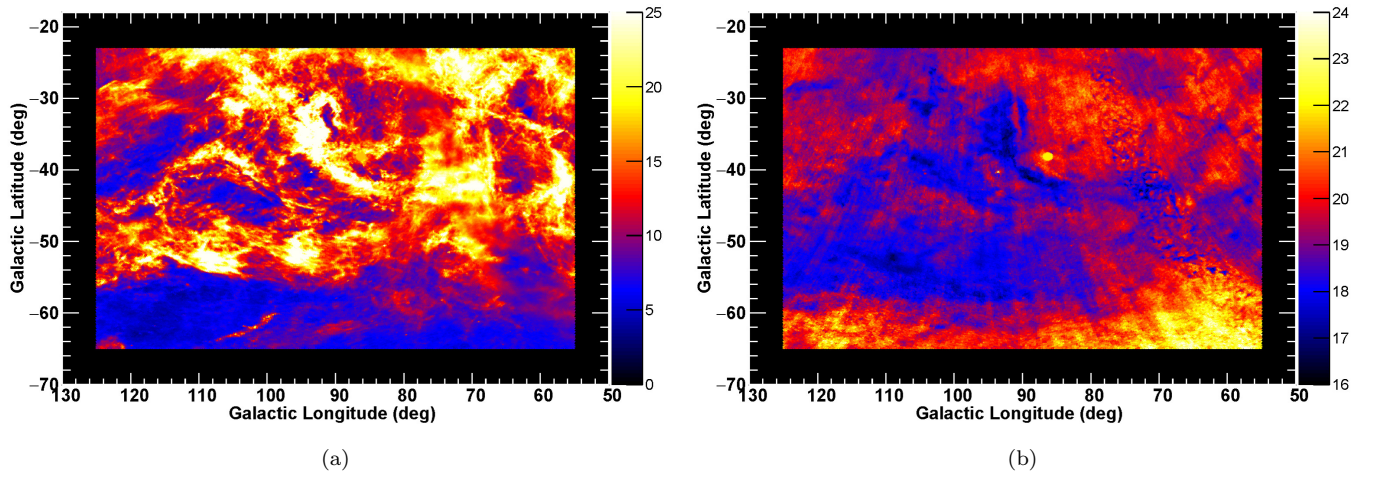


**Figure 2.** (a) The dust  $R$  map ( $10^{-8} \text{ W m}^{-2} \text{ sr}^{-1}$ ); (b) the  $T_d$  map (K). Both maps are from *Planck* Data Release 1, and the infrared sources are masked as described in Appendix A.

### 3. GAMMA-RAY DATA AND MODELING

#### 3.1. *Gamma-ray Observations and Data Selection*

The LAT on board the *Fermi Gamma-ray Space Telescope*, launched in 2008 June, is a pair-tracking  $\gamma$ -ray telescope that detects photons in the range from  $\sim 20$  MeV to more than 300 GeV. Details of the LAT instrument and the pre-launch performance expectations can be found in [Atwood et al. \(2009\)](#), and the on-orbit calibration is described in [Abdo et al. \(2009a\)](#). Thanks to its wide field of view ( $\sim 2.4$  sr), *Fermi*-LAT is an ideal telescope to use for studying Galactic diffuse  $\gamma$ -rays. Although the angular resolution is worse than those of gas tracers and energy dependent (68% containment radii<sup>5</sup> are  $\sim 5^\circ$  and  $0.8^\circ$  at 100 MeV and 1 GeV, respectively), it will be taken into account in the  $\gamma$ -ray data analysis described in Section 3.3. Past studies of Galactic diffuse emission by *Fermi*-LAT can be found in, e.g., [Ackermann et al. \(2012a\)](#) and [Casandjian \(2015\)](#).

Routine science operations with the LAT started on 2008 August 4. We have accumulated events from 2008 August 4 to 2020 August 3 (i.e., 12 years) to study diffuse  $\gamma$ -rays in our ROI ( $60^\circ \leq l \leq 120^\circ$  and  $-60^\circ \leq b \leq -28^\circ$ ). During most of this time interval, the LAT was operated in sky-survey mode, obtaining complete sky coverage every two orbits (which corresponds to  $\sim 3$  h), with relatively uniform exposure over time. We used the latest release of the Pass 8 ([Atwood et al. 2013](#); [Bruel et al. 2018](#)) data (P8R3), which is less contaminated by a residual background than previous ones. We used the standard LAT analysis software, *Fermitools*<sup>6</sup> version 2.0.0, to select events satisfying the ULTRACLEAN class in order to obtain low-background events. We also required that the reconstructed zenith angles of the arrival directions of the photons be less than  $100^\circ$  and  $90^\circ$  for energies above and below 300 MeV, respectively, to reduce contamination by photons from Earth's atmosphere. To accommodate the relatively poor angular resolution at low energy, we used events and the responses of point-spread-function (PSF) event types 2 and 3 below 300 MeV. However, above 300 MeV, we did not apply selections based on PSF event types to maximize the photon statistics. We used the `gtselect` command to apply the selections described above.

In addition, we referred to the Monitored Source List light curves<sup>7</sup>, and by using the `gtmktime` command, we excluded the periods ( $\sim 1600$  days in total) during which the LAT detected flares from 3C 454.3. This significantly reduced contamination in the diffuse emission from the bright active galactic nucleus. The count-rate threshold was more stringent than that used in [Mizuno et al. \(2016\)](#) in order to reduce the contamination better.<sup>8</sup> We also excluded the periods during which the LAT detected bright  $\gamma$ -ray bursts or solar flares. (The integrated time excluded in this procedure is negligible compared to that excluded to remove data with flares from 3C 454.3.) Then we prepared a livetime cube by using the `gtltcube` command. We used the latest response functions that match our dataset and event selection, P8R3\_ULTRACLEAN\_V3, in the following analysis.

As described in Section 3.2, we carried out a bin-by-bin likelihood fitting and took account of the energy dispersion. Using the latest P8R3 data, applying a tighter cut to the 3C454.3 flares, using PSF event types, and taking account of the energy dispersion are major improvements in data selection and fitting, allowing us to lower the minimum energy used in the analysis down to 100 MeV.

#### 3.2. *Model to Represent the Gamma-ray Emission*

We modeled the  $\gamma$ -ray emission observed by *Fermi*-LAT as a linear combination of the gas column density maps, IC emission, an isotropic component, and  $\gamma$ -ray point sources. The use of the gas column density maps as templates is based on the assumption that  $\gamma$ -rays are generated via interactions between the CRs and ISM gas and that CR intensities do not vary significantly over the scale of the interstellar complexes in this study. This assumption is simple but plausible, particularly in high Galactic latitude regions such as the one studied here, as has been verified by past studies of local clouds using *Fermi*-LAT data (for a review, see, e.g., [Grenier et al. 2015](#)). As described in Section 4, we started with three  $N_{\text{HI}}$  maps derived from the  $W_{\text{HI}}$  maps (assuming that the HI is optically thin) and a  $W_{\text{CO}}$  map (see Section 2). We then improved the templates by using the dust-emission ( $D_{\text{em}}$ ) model maps. We used the  $\gamma$ -ray emissivity model adopted in [Abdo et al. \(2009b\)](#) to calculate the  $\gamma$ -ray emissivity. To model the  $\gamma$ -rays produced via IC scattering, we used GALPROP<sup>9</sup> (e.g., [Strong & Moskalenko 1998](#); [Strong et al. 2007](#)). GALPROP is a numerical code that solves the CR transport equation within the Galaxy and predicts the  $\gamma$ -ray emission produced

<sup>5</sup> Radius of a circle in which 68% of photons from a source are contained

<sup>6</sup> <https://fermi.gsfc.nasa.gov/ssc/data/analysis/software/>

<sup>7</sup> <https://fermi.gsfc.nasa.gov/ssc/data/access/lat/msslc/>

<sup>8</sup> The lists of the mission elapsed time (the number of seconds since 2001 January 1) that passed the criteria are 2.45–2.72, 3.23–4.17, 5.05–5.45, and larger than 5.47 in  $10^8$ .

<sup>9</sup> <http://galprop.stanford.edu>

via the interactions of CRs with interstellar matter and with low-energy photons (IC scattering). It calculates the IC emission from the distribution of propagated electrons and the interstellar radiation field. Specifically, we utilized the recent work by Porter et al. (2017). After testing several IC models against the  $\gamma$ -ray data with our baseline gas model (three  $N_{\text{HI}}+W_{\text{CO}}$  templates), we decided to use an IC model based on a conventional CR distribution and the ISRF (SAO-Std model in Porter et al. (2017)); see Appendix B for details. To model the individual  $\gamma$ -ray point sources, we referred to the fourth *Fermi*-LAT catalog (4FGL) described in Abdollahi et al. (2019), which is based on the first 8 years of the science phase of the mission and includes more than 5000 sources detected at a significance level of  $\geq 4\sigma$ . For our analysis, we considered 128 4FGL sources (detected at a significance level  $\geq 5\sigma$ ) in our ROI. In addition, we included bright sources ( $\geq 20\sigma$ ) just outside it (within  $10^\circ$ ), with the parameters fixed at those in the 4FGL, to consider their possible contamination. We also added an isotropic component to represent the extragalactic diffuse emission and the residual instrumental background from misclassified CR interactions in the LAT detector. We adopted the isotropic template provided by the *Fermi* Science Support Center<sup>10</sup>.

Then, the  $\gamma$ -ray intensities  $I_\gamma(l, b, E)$  ( $\text{ph s}^{-1} \text{cm}^{-2} \text{sr}^{-1} \text{MeV}^{-1}$ ) can be modeled as

$$I_\gamma(l, b, E) = \left[ \sum_i C_{\text{HI},i}(E) \cdot N_{\text{HI},i}(l, b) + C_{\text{CO}}(E) \cdot 2X_{\text{CO}}^0 \cdot W_{\text{CO}}(l, b) + C_{\text{dust}}(E) \cdot X_{\text{dust}}^0 \cdot D_{\text{em}}(l, b) \right] \cdot q_\gamma(E) \quad (1)$$

$$+ C_{\text{IC}}(E) \cdot I_{\text{IC}}(l, b, E) + C_{\text{iso}}(E) \cdot I_{\text{iso}}(E) + \sum_j \text{PS}_j(l, b, E) \quad ,$$

where the  $N_{\text{HI},i}$  is the atomic gas column density ( $\text{cm}^{-2}$ ) model maps,  $q_\gamma$  ( $\text{ph s}^{-1} \text{sr}^{-1} \text{MeV}^{-1}$ ) is the model of the differential  $\gamma$ -ray yield or  $\gamma$ -ray emissivity per H atom,  $W_{\text{CO}}$  is the integrated  $^{12}\text{CO}$  ( $J=1-0$ ) intensity map ( $\text{K km s}^{-1}$ ),  $D_{\text{em}}$  is the dust-emission model ( $R$  or  $\tau_{353}$ ), which is a tracer of the total gas column density (see Section 4.1) or the residual gas (see Section 4.2).  $R$  and  $\tau_{353}$  are given in  $\text{W m}^{-2} \text{sr}^{-1}$  and optical depth, respectively. The quantities  $I_{\text{IC}}$  and  $I_{\text{iso}}$  are the IC model and the isotropic template intensities ( $\text{ph s}^{-1} \text{cm}^{-2} \text{sr}^{-1} \text{MeV}^{-1}$ ), respectively, and  $\text{PS}_j$  represents the point-source contributions. The subscript  $i$  allows for the use of  $N_{\text{HI}}$  maps from separate H I line profiles. We adopted the  $\gamma$ -ray emissivity model used in Abdo et al. (2009b). To accommodate the uncertainties, in either the emissivity model or the gas templates, we included normalization factors [ $C_{\text{HI},i}$ ,  $C_{\text{CO}}$ , or  $C_{\text{dust}}$  in Equation (1)] as free parameters. The quantities  $X_{\text{CO}}^0$  and  $X_{\text{dust}}^0$  are constant scale factors used to make the fitting coefficients ( $C_{\text{CO}}$  and  $C_{\text{dust}}$ ) close to 1. Specifically, we used  $1 \times 10^{20} \text{cm}^{-2} (\text{K km s}^{-1})^{-1}$  and  $1.82 \times 10^{28} \text{cm}^{-2} (\text{W m}^{-2} \text{sr}^{-1})^{-1}$  for  $X_{\text{CO}}^0$  and  $X_{\text{dust}}^0$  (for  $R$ ), respectively. While  $C_{\text{HI},i}$  will be 1 if  $N_{\text{HI},i}$  represents the true gas column density and the  $\gamma$ -ray emissivity agrees with the adopted model,  $C_{\text{CO}}$  and  $C_{\text{dust}}$  provide the CO-to-H<sub>2</sub> conversion factor ( $X_{\text{CO}} \equiv N_{\text{H}_2}/W_{\text{CO}}$ , where  $N_{\text{H}_2}$  gives the molecular gas column density) and the dust-to-gas conversion factor, respectively.  $X_{\text{CO}}$  will be  $X_{\text{CO}}^0$  if  $C_{\text{HI},i}$  for optically thin H I ( $C_{\text{HI},3}$  as will be described in Section 4.1) and  $C_{\text{CO}}$  are equal [ $X_{\text{CO}} = X_{\text{CO}}^0 \times (C_{\text{CO}}/C_{\text{HI},3})$ ]. The IC emission and isotropic models (see above) also are uncertain, and we have therefore included other normalization factors [the quantities  $C_{\text{IC}}$  and  $C_{\text{iso}}$  in Equation (1)] as free parameters. For the point sources, we adopted spectral models in the 4FGL; the spectral parameter of normalization was set to be free, and other spectral parameters and the positions of each source were fixed at the values in the 4FGL. We divided the  $\gamma$ -ray data into several energy ranges and fitted Equation (1) to the  $\gamma$ -rays in each energy range using the binned-likelihood method, with energy dispersion taken into account, both implemented in *Fermitools*.

### 3.3. Model-Fitting Procedure

We divided the  $\gamma$ -ray data into 10 energy bands extending from 0.1 to 72.9 GeV and stored them in HEALPix maps of order 8 (by using the `gtbin` command). We used a pixel size a factor of 2 larger than those of the gas maps (Section 2) to accommodate for the small photon statistics, while keeping the  $\gamma$ -ray map fine enough to evaluate the gas distribution of H I. We used energy bins equally spaced logarithmically for the first eight bands (e.g., 0.1–0.17, 0.17–0.3, and 0.3–0.52 GeV) and employed bins twice as broad for the last two bands to accommodate for the small photon statistics. To evaluate the model spectral shape, the data were subdivided into three (six) grids within the narrower (broader) energy bands. Then, in each energy band, we prepared exposure and source maps with finer grids taken into account (by using the `gtexpcube2` and `gtsrcmaps` commands), and fitted Equation (1) to the  $\gamma$ -ray data using the binned maximum-likelihood method with Poisson statistics implemented in *Fermitools* (by importing the

<sup>10</sup> <https://fermi.gsfc.nasa.gov/ssc/data/access/lat/BackgroundModels.html>

`BinnedAnalysis` module in python). The angular resolution of  $\gamma$ -ray data is taken into account in this step. Since the angular resolutions of the gas maps are much better than that of  $\gamma$ -ray data in most of the energy range investigated, gas maps are convolved with the angular resolution of *Fermi*-LAT in the  $\gamma$ -ray data analysis. Also, since the statistical errors of the  $\gamma$ -ray data is much larger than the errors of the gas tracer intensity in most pixels, we do not take into account the latter in fitting the  $\gamma$ -ray data. We modeled  $C_{\text{HI},i}$ ,  $C_{\text{CO}}$ ,  $C_{\text{dust}}$ ,  $C_{\text{IC}}$ , and  $C_{\text{iso}}$  as energy-independent normalization factors in each energy band, and we modeled  $\text{PS}_j$  with only the normalization free to vary.

When modeling the point sources, we first sorted them (total 128 sources) by significance and divided them into 13 groups (each group has 10 sources at the maximum). We then iteratively fitted them in order of decreasing significance. First, we fitted the normalizations of the 10 most significant sources; then, we fitted the normalizations of the second group with parameters of the first group fixed at the values already determined. In this way, we worked down to the sources detected at more than  $5\sigma$  in 4FGL. For each step, the parameters of the diffuse-emission model were always left free to vary. After we reached the least-significant sources, we went back to the brightest ones and let them and the diffuse-emission models be free to vary while the parameters of the other sources were kept fixed at the values already determined. We repeated this process until the increments of the log-likelihoods,  $\ln L$ <sup>11</sup>, were less than 0.1 over one loop in each energy band.

<sup>11</sup>  $L$  is conventionally calculated as  $\ln L = \sum_i n_i \ln(\theta_i) - \sum_i \theta_i$ , where  $n_i$  and  $\theta_i$  are the data and the model-predicted counts in each pixel (for each energy grid) denoted by the subscript, respectively (see, e.g., [Mattox et al. 1996](#)).

#### 4. DATA ANALYSIS

Most of past  $\gamma$ -ray analyses used HI data (single map or maps sorted by velocity),  $W_{\text{CO}}$  data, and dust data. The novelty of this work is to use HI linewidth information in preparing  $N_{\text{HI}}$  maps. Specifically, we prepared  $N_{\text{HI}}$  maps of narrow HI and broad HI (Section 2) and assumed that the latter traces optically thin HI. As will be described in Section 4.1, we expect that narrow HI traces dark gas and confirm our expectation. We also find that there remains residual gas and employ a dust map to trace them (Section 4.2). Final modeling is described in Section 4.3.

##### 4.1. Initial Modeling

To examine how well the narrow HI traces the dark gas, either optically thick HI (directly) or CO-dark  $\text{H}_2$  (indirectly), we started our analysis of  $\gamma$ -ray data [Figure 3(a)] using the three HI maps and the  $W_{\text{CO}}$  map shown in Figure 1 (hereafter called the “baseline model”) as gas templates. This is equivalent to setting  $C_{\text{dust}} = 0$  in Equation (1), while other coefficients ( $C_{\text{HI},i}$  and  $C_{\text{CO}}$ ) are free to vary. Hereafter, we will use  $C_{\text{HI},1}$ ,  $C_{\text{HI},2}$ , and  $C_{\text{HI},3}$  to represent the fit coefficients for IVC, narrow HI, and broad HI, respectively. We adopted the optically thin approximation to convert  $W_{\text{HI}}$  into  $N_{\text{HI}}$ . If broad HI and narrow HI, respectively, trace the optically thin HI and the dark gas (either optically thick HI or CO-dark  $\text{H}_2$ ) well, we will have a larger emissivity for the latter and a flat fit-residual. Indeed, we observed that narrow HI gives about 2 times larger emissivity ( $C_{\text{HI},2} \sim 2C_{\text{HI},3}$ ). However, we found that our baseline model shows coherent residuals<sup>12</sup> in both the MBM 53-55 clouds and the Pegasus loop, as shown in Figure 3(b). There, we overlaid contours of  $R = 18 \times 10^{-8} \text{ W m}^{-2} \text{ sr}^{-1}$  to indicate ISM structures. Considering that *Fermi*-LAT has a very large field of view and has continuously scanned the whole sky for more than a decade and is well calibrated accordingly (Section 3.1), such residuals cannot be attributed to the instrumental uncertainty of the  $\gamma$ -ray data. This indicates that our baseline model does not fully trace all the neutral gas, particularly in those ISM structures. We also applied a  $T_{\text{D}}$ -dependent correction proposed by Kalberla et al. (2020) [Equation (7) in their paper] to the (narrow + broad HI) map to construct the summed column density map and used it to fit the  $\gamma$ -ray data. However, we obtained a residual very similar to that in Figure 3(b). Therefore, some fraction of gas is missed by HI 21-cm lines, even if we adopt the  $T_{\text{D}}$ -dependent correction by Kalberla et al. (2020). This motivates us to employ a dust map to model this residual gas. To determine which dust model to use, we tested single model maps of the total gas column density ( $N_{\text{H}}^{\text{tot}}$ ) proportional to  $R$  or  $\tau_{353}$  (from *Planck* Data Release 1 and 2). This is equivalent to setting  $C_{\text{HI},i} = 0$  and  $C_{\text{CO}} = 0$ . Although there are fewer degrees of freedom, each dust map gives a larger value of  $\ln L$  than does our baseline gas model. Therefore, we concluded that we can use a dust map to estimate the residual gas not accounted for by HI lines or  $W_{\text{CO}}$ . We interpret this residual gas being CO-dark  $\text{H}_2$ . Since both  $\tau_{353}$  and  $R$  have potential issues as a tracer of the total gas column density (see, e.g., Mizuno et al. 2016, and references therein), we referred to  $\ln L$  to determine which dust model to use. We found that the  $R$  map from *Planck* Data Release 1 gives the best fit among four “single gas model maps”, and hence we use it to construct the residual gas template. In the following section, we will construct a residual gas template and also examine if a model with the residual gas template gives a better fit than the model using a single dust map.

##### 4.2. Fit with the Residual-Gas Template

Having confirmed that our baseline gas model (the three  $W_{\text{HI}}$  maps, divided by using the HI line profiles, and the  $W_{\text{CO}}$  map) is not good enough to reproduce the  $\gamma$ -ray data, we add a residual gas template obtained by using the  $R$  map from *Planck* Data Release 1. To construct a good template, we examined the correlations among the HI,  $W_{\text{CO}}$ , and the dust maps in our ROI stored in a HEALPix map of order 9 (see Section 2). To match the resolution of the  $W_{\text{HI}}$  map, we smoothed the dust maps using a Gaussian kernel with an FWHM of  $15'.4$ . Since  $W_{\text{CO}}$  data has a worse resolution and covers a small fraction of the ROI, we kept the original resolution for it. Then, by studying the gas properties in detail, we removed gas phases other than the residual gas from HI and  $R$  data, and constructed the residual gas template as follows. To reduce contamination from CO-bright  $\text{H}_2$ , we required  $W_{\text{CO}} \leq 0.1 \text{ K km s}^{-1}$ , except in the third step (subtraction of CO-bright  $\text{H}_2$ ). Unlike HI data, we cannot distinguish different gas phases in a dust map along the line of sight using velocity information. Instead, we use  $T_{\text{d}}$  to best separate gas phases as described below. We aim to identify optically thin HI and since  $\gamma$ -ray data have been generally reproduced by models using HI column densities assuming high  $T_{\text{s}}$  ( $\geq 125 \text{ K}$ ),  $W_{\text{CO}}$ , and a residual gas template (see, e.g., Remy et al. 2017, and references therein), we assume linearity between  $W_{\text{HI}}$  and  $R$  at this stage.

<sup>12</sup> Specifically, we refer to residuals at around  $(l, b) \sim (96^\circ, -35^\circ)$ ,  $(105^\circ, -38^\circ)$ ,  $(103^\circ, -40.5^\circ)$ ,  $(116^\circ, -51^\circ)$ , and  $(108^\circ, -54^\circ)$ . They positionally coincide with the MBM 53-55 clouds and the Pegasus loop seen in narrow HI map [Figure 1(b)] and dust  $R$  map [Figure 2(a)].

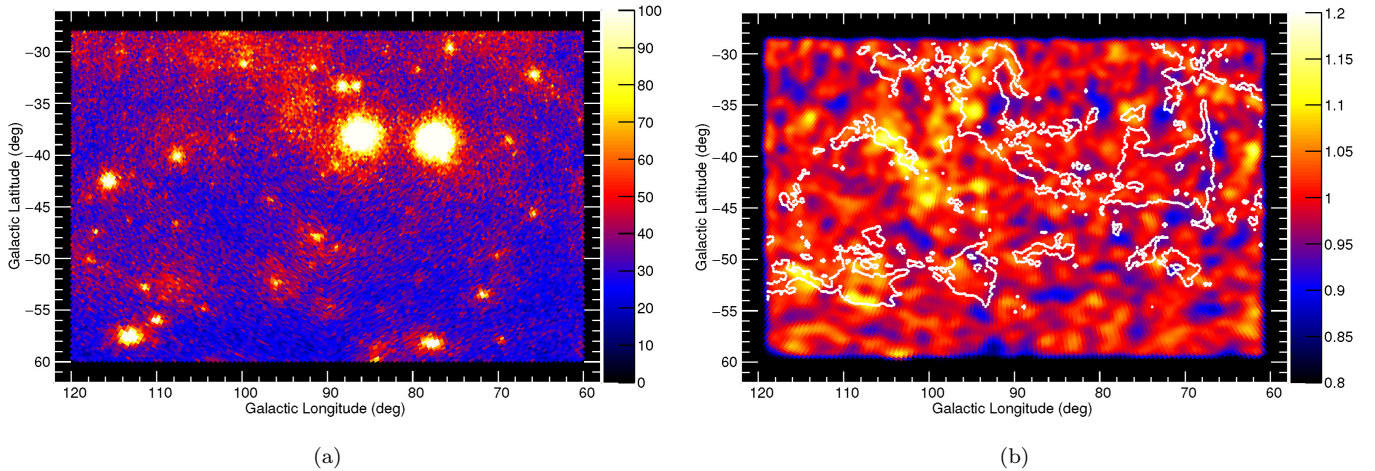


**Figure 3.** (a) The data count map. (b) The data/model ratio map using the baseline gas model. To accommodate small photon statistics (large statistical errors), the panel (b) was smoothed using a Gaussian kernel with a standard deviation  $\sigma = 60'$ . Contours of  $R = 18 \times 10^{-8} \text{ W m}^{-2} \text{ sr}^{-1}$  are overlaid to indicate ISM structures.

### Subtraction of IVCs:

We examined the  $W_{\text{HI}}(\text{total})$  vs.  $R(\text{total})$  correlation and found that the outliers in the correlation at around  $R$  ( $10^{-8} \text{ W m}^{-2} \text{ sr}^{-1}$ )  $\sim 10$  and  $W_{\text{HI}}$  ( $\text{K km s}^{-1}$ )  $\sim 350$  are affected by IVCs, as shown in Figure 4(a). Most of the pixels with a high IVC fraction (i.e., the fractional  $W_{\text{HI}}$  of the IVC is more than 25%, represented by the green points) exhibit higher  $W_{\text{HI}}/R$  ratios than the average. We understand that this is because IVCs in our ROI are dust poor (e.g., Fukui et al. 2021). While the true  $W_{\text{HI}}/R$  ratio of the IVCs is uncertain, their contribution to the gas density is small (integral of  $W_{\text{HI}}$  is at the 5% level; see Mizuno et al. 2016). Therefore, for simplicity, we removed the IVCs from the  $W_{\text{HI}}$  and  $R$  maps, assuming that they do not have dust (i.e., we subtracted the column density of the IVCs from  $W_{\text{HI}}$ , while keeping the value of  $R$  for each pixel). Unchanging  $R$  would overestimate the other gas component, but the effect is minor since IVCs' contribution is small and their spatial distribution [Figure 1(a)] is very different from that of other gas phases. Now we have a  $W_{\text{HI}}$  map of narrow and broad HI (hereafter called  $W_{\text{HI},2+3}$ ).

### Subtraction of broad HI:

Then we examined the  $W_{\text{HI},2+3}$  vs.  $R(\text{total})$  correlation [Figure 4(b)]. We first aimed to evaluate  $R/W_{\text{HI}}$  ratio of broad HI, and selected areas rich in broad HI (i.e., with the fractional  $W_{\text{HI}}$  of broad HI more than 95%). Narrow HI will have a larger  $N_{\text{H}}/W_{\text{HI}}$  ratio (where  $N_{\text{H}}$  is the column density of each gas phase) than broad HI does if it is optically thick. CO-dark  $\text{H}_2$  will have an even larger  $N_{\text{H}}/W_{\text{HI}}$  ratio. They will have larger  $R/W_{\text{HI}}$  ratio, and may not be removed well by the  $W_{\text{HI}}$ -based selection. Such an excess gas (over optically thin HI) has been found towards the directions of low  $T_{\text{d}}$  (e.g., Mizuno et al. 2016; Hayashi et al. 2019). As described in Fukui et al. (2014), both the HI gas and dust are heated by ISRF and hence are expected to have a positive correlation between their temperatures. Therefore optically thick HI will be found primarily in the low- $T_{\text{d}}$  area. CO-dark  $\text{H}_2$  could also have a similar dependence on  $T_{\text{d}}$ .

Therefore, to further reduce the possible contamination from optically thick HI and CO-dark  $\text{H}_2$ , we also required these areas to have  $T_{\text{d}} \geq 20 \text{ K}$  (the red points in the panel). We then calculated the average of  $W_{\text{HI}}$  and  $R$  in every  $40 \text{ K km s}^{-1}$  bin from  $W_{\text{HI}} = 100$  to  $300 \text{ K km s}^{-1}$  and obtained the linear relation  $R$  ( $10^{-8} \text{ W m}^{-2} \text{ sr}^{-1}$ ) =  $0.0463 \cdot W_{\text{HI}}$  ( $\text{K km s}^{-1}$ ). We interpret this gives the  $R/W_{\text{HI}}$  ratio of broad HI gas and subtracted them from the  $W_{\text{HI},2+3}$  and  $R(\text{total})$  maps using this ratio. We note that changing the threshold of  $T_{\text{d}}$  by  $\pm 1 \text{ K}$  affects the ratio less than 5%, confirming that a specific choice of the  $T_{\text{d}}$  threshold does not affect the final map significantly. Now we have a  $W_{\text{HI}}$  map of narrow HI ( $W_{\text{HI},2}$ ), and an  $R$  map associated with narrow HI, CO-bright and the residual gas ( $R_{2+\text{CO}+\text{res}}$ ).

### Subtraction of CO-bright H<sub>2</sub>:

We then examined the  $W_{\text{CO}}$  and  $R_{2+\text{CO}+\text{res}}$  correlation. To select  $W_{\text{CO}}$ -rich areas, we required  $W_{\text{CO}}$  to be greater than  $1 \text{ K km s}^{-1}$ . We then calculated the averages of  $W_{\text{CO}}$  and  $R$  in every  $2 \text{ K km s}^{-1}$  bin from  $W_{\text{CO}} = 1$  to  $12 \text{ K km s}^{-1}$  (the last bin spans from 9 to  $12 \text{ K km s}^{-1}$ ) and fitted them with a linear relation with offset. Since dark gas lies around CO clouds (e.g., Grenier et al. 2005), their contribution will be mainly attributed to the offset. We obtained the linear relation  $R (10^{-8} \text{ W m}^{-2} \text{ sr}^{-1}) = 18.5 + 1.95 \cdot W_{\text{CO}} (\text{K km s}^{-1})$ , and subtracted the CO-bright H<sub>2</sub> gas from the  $R_{2+\text{CO}+\text{res}}$  map using the obtained coefficient. Although there is a significant scatter in Figure 4(c) and hence the uncertainty of  $R/W_{\text{CO}}$  ratio is large, the effect on the ISM gas properties is small (except CO-bright H<sub>2</sub>) as will be described in Section 5.1. Now we have an  $R$  map associated with narrow HI and the residual gas ( $R_{2+\text{res}}$ ).

### Subtraction of narrow HI:

The correlation between the  $W_{\text{HI},2}$  and  $R_{2+\text{res}}$ , sorted by  $T_{\text{d}}$  is shown in Figure 4(d). In order to remove narrow HI gas, we first aimed to evaluate  $R/W_{\text{HI}}$  ratio of it. In Figure 4(d), we found that areas with low  $T_{\text{d}}$  exhibit a high  $R/W_{\text{HI}}$  ratio, which we interpret as being the residual gas we found in Section 4.1. To reduce their contamination, we selected high- $T_{\text{d}}$  areas ( $T_{\text{d}}$  more than 20 K). We then calculated the average of  $W_{\text{HI}}$  and  $R$  in every  $30 \text{ K km s}^{-1}$  bin from  $W_{\text{HI}} = 0$  to  $150 \text{ K km s}^{-1}$ , and we obtained the linear relation  $R (10^{-8} \text{ W m}^{-2} \text{ sr}^{-1}) = 0.0705 \cdot W_{\text{HI}} (\text{K km s}^{-1})$ . We removed narrow HI from the  $R_{2+\text{res}}$  map using this ratio. Now we have the residual gas template and we use it in the  $\gamma$ -ray data analysis. If  $T_{\text{s}}$  is high throughout HI, as claimed by several past studies, this analysis will give similar emissivities for broad and narrow HI templates.

The residual gas template improves the fit significantly; the residuals seen in the MBM 53-55 clouds and the Pegasus loop are reduced significantly, and the value of  $\ln L$  increased by 337.5 with 10 degrees of freedom. Therefore the residual gas template successfully reproduces the gas not traced by our baseline model. The model with the residual gas template gives  $\Delta \ln L = 103.4$  with 20 more degrees of freedom than the model using single  $R$  (of *Planck* Data Release 1). We also found that narrow HI gives about 1.5 times larger emissivity than that of broad HI ( $C_{\text{HI},2} \sim 1.5C_{\text{HI},3}$ ). We understand that this is because narrow HI is optically thick, and we apply a correction for this in calculating the gas column density.

#### 4.3. Final Modeling with $T_{\text{s}}$ corrections

We applied a spin-temperature correction to the gas column density based on Fukui et al. (2014) and Hayashi et al. (2019) to construct a new narrow HI template and a residual gas template. For simplicity, we assumed that the peak brightness temperature ( $T_{\text{p}}$ ) is representative of the brightness temperature along the line of sight. Then, the radiation transfer equation gives  $W_{\text{HI}}$  and the optical depth  $\tau_{\text{HI}}$  of the HI gas as a function of  $T_{\text{s}}$  and  $\Delta V_{\text{HI}} (\equiv W_{\text{HI}}/T_{\text{p}})$  as

$$W_{\text{HI}} (\text{K km s}^{-1}) = [T_{\text{s}} (\text{K}) - T_{\text{bg}} (\text{K})] \cdot \Delta V_{\text{HI}} (\text{km s}^{-1}) \cdot [1 - \exp(-\tau_{\text{HI}})] , \quad (2)$$

and

$$\tau_{\text{HI}} = \frac{N_{\text{HI}} (\text{cm}^{-2})}{1.82 \times 10^{18}} \cdot \frac{1}{T_{\text{s}} (\text{K})} \cdot \frac{1}{\Delta V_{\text{HI}} (\text{km s}^{-1})} , \quad (3)$$

where  $T_{\text{bg}}$  is the background continuum radiation temperature and  $N_{\text{HI}}$  is the gas column density of HI gas. Then, we can calculate  $N_{\text{HI}}$  as

$$N_{\text{HI}} = -1.82 \times 10^{18} \cdot T_{\text{s}} (\text{K}) \cdot \Delta V_{\text{HI}} (\text{km s}^{-1}) \cdot \log \left[ 1 - \frac{W_{\text{HI}} (\text{K km s}^{-1})}{[T_{\text{s}} (\text{K}) - T_{\text{bg}} (\text{K})] \cdot \Delta V_{\text{HI}} (\text{km s}^{-1})} \right] . \quad (4)$$

We calculated the value of  $N_{\text{HI}}$  for narrow HI using Equation (4), assuming a uniform  $T_{\text{s}}$  over the ROI and  $T_{\text{bg}} = 2.7 \text{ K}$  (the temperature of the cosmic microwave background radiation). We note that using a single brightness temperature along the line of sight and a uniform  $T_{\text{s}}$  over the ROI is a rough approximation that may introduce over- or under-prediction at the pixel level. Also, we compared data and model of Gaussian decomposition for several pixels with a complex profile (the number of Gaussians more than 7; see Kalberla & Haud 2018) and found that parameters of narrow lines could be affected by dominant broad lines there. Therefore, the value of  $T_{\text{s}}$  should not be taken at face value. It is a reasonable approach, though, considering the low photon statistics of the  $\gamma$ -ray data. Also, it allows us for the first time to apply different  $T_{\text{s}}$  corrections to the different HI gas phases used in the  $\gamma$ -ray data analysis.

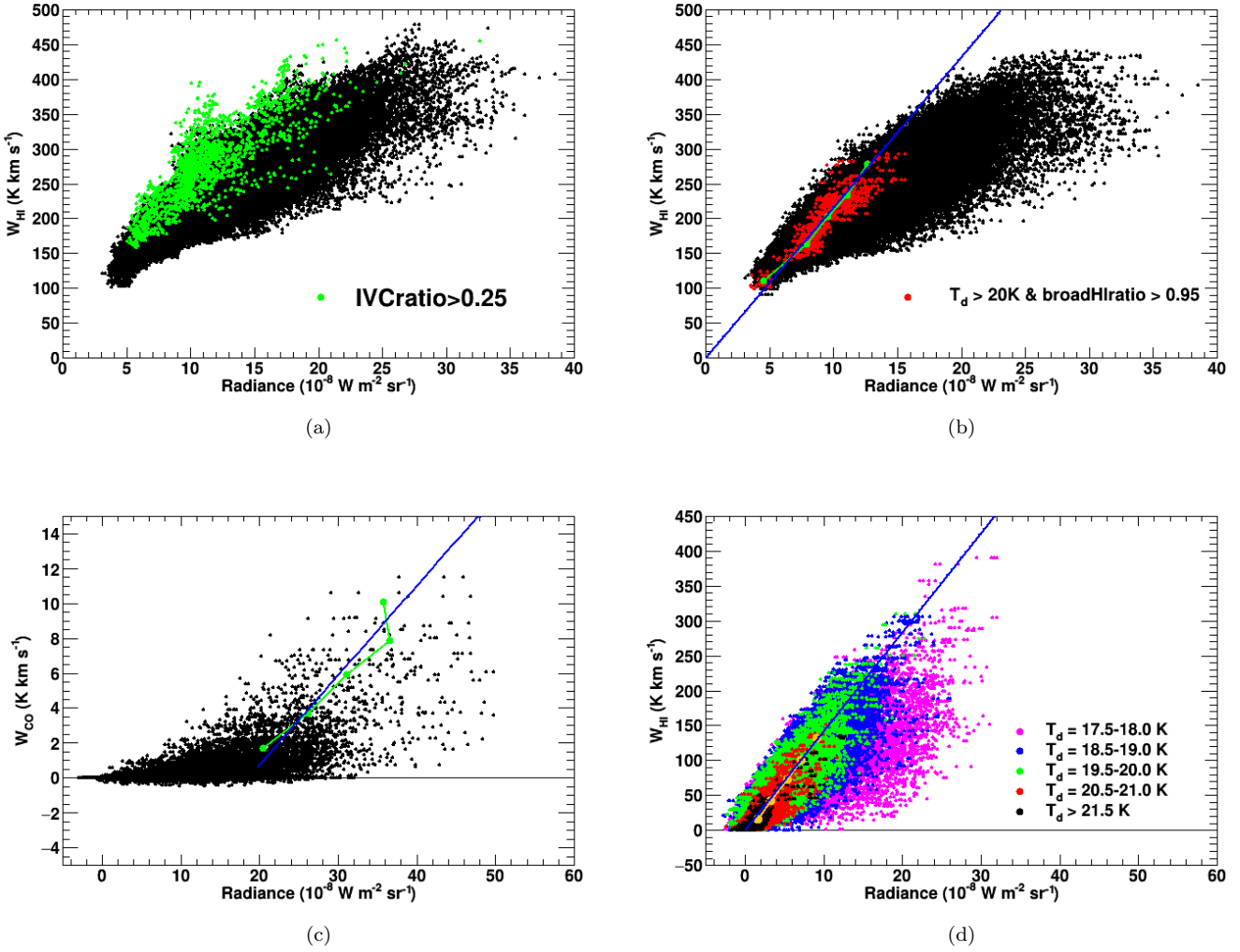


**Figure 4.** Correlation of ISM gas in our ROI. Each point represents each pixel of our HEALPix map. (a) The  $W_{\text{HI}}(\text{total})-R(\text{total})$  correlation. Pixels with large IVC fractions are colored green. (b) The  $W_{\text{HI},2+3}-R(\text{total})$  correlation after subtracting the IVCs. Areas with large broad H I fractions and high  $T_d$  are colored red. The averages of  $W_{\text{HI}}$  and  $R$  in  $W_{\text{HI}}$  bins are shown by green points. (c) The  $W_{\text{CO}}-R_{2+\text{CO}+\text{res}}$  correlation after subtracting broad H I. The averages of  $W_{\text{CO}}$  and  $R$  in  $W_{\text{CO}}$  bins are shown by green points. (d) The  $W_{\text{HI},2}-R_{2+\text{res}}$  correlation after subtracting CO-bright  $\text{H}_2$ . Data are shown in 0.5 K ranges of  $T_d$  with 0.5 K gaps between intervals for clarity. The averages of  $W_{\text{HI}}$  and  $R$  in  $W_{\text{HI}}$  bins are shown by orange points. In panels (b), (c), and (d), the best fit linear relations are shown by blue lines. To reduce contamination from CO-bright  $\text{H}_2$ , we required  $W_{\text{CO}} \leq 0.1 \text{ K km s}^{-1}$  except in panel (c). See text for details of the procedures used to construct the residual-gas template.

We constructed  $N_{\text{HI}}$  maps of narrow H I assuming  $T_s = 120$  to 30 K in 10 K steps. If  $T_p > T_s - T_{\text{bg}}$ , Equation (4) diverges to infinity. In such a case, we stopped at  $T_s$  that gives  $\tau_{\text{HI}} = 3$  in Equation (2), and calculated  $N_{\text{HI}}$  using Equation (4).  $T_p > T_s - T_{\text{bg}}$  only in a small fraction of pixels (less than 0.1%) for  $T_s \leq 40$  K. We then constructed a residual gas template for each  $T_s$ . Specifically, we replaced  $W_{\text{HI}}$  in Figure 4(d) with  $N_{\text{HI}}(\text{cm}^{-2})/(1.82 \times 10^{18})$ . Although the difference in  $\ln L$  is small, we confirmed that the fit improves gradually as we apply corrections with lower values of  $T_s$  down to  $T_s = 40$  K. We therefore concluded that the templates with a  $T_s$  correction of 40 K applied to narrow H I represent our best model, and we adopted them as our final model. The emissivity of narrow H I now agrees with that of broad H I at the 10% level. Specifically, the averages of  $C_{\text{HI},2}$  (narrow H I) and  $C_{\text{HI},3}$  (broad H I) are  $0.980 \pm 0.018$  and  $0.866 \pm 0.030$ , respectively, giving the ratio of narrow H I : broad H I = 1.13. The model count map and the data/model ratio map are shown in Figure 5. By comparison with Figure 3, we can confirm that the residuals are reduced significantly. A summary of the emissivity spectrum and the spectrum of each component are presented

in Figure 6, and the best-fit parameters are summarized in Table 1. Although the spectral shape of CO-bright H<sub>2</sub> and IVC is apparently different from those of other gas templates, they are minor components and the errors are large, and hence the effect on other components is small. Also, although the IC spectrum shows unphysical fluctuation, it anticorrelates with the isotropic spectrum. Therefore, most of uncertainties of the IC and the isotropic emission (both have smooth spatial distributions) are mutually absorbed and have small impact on gas emissivities.

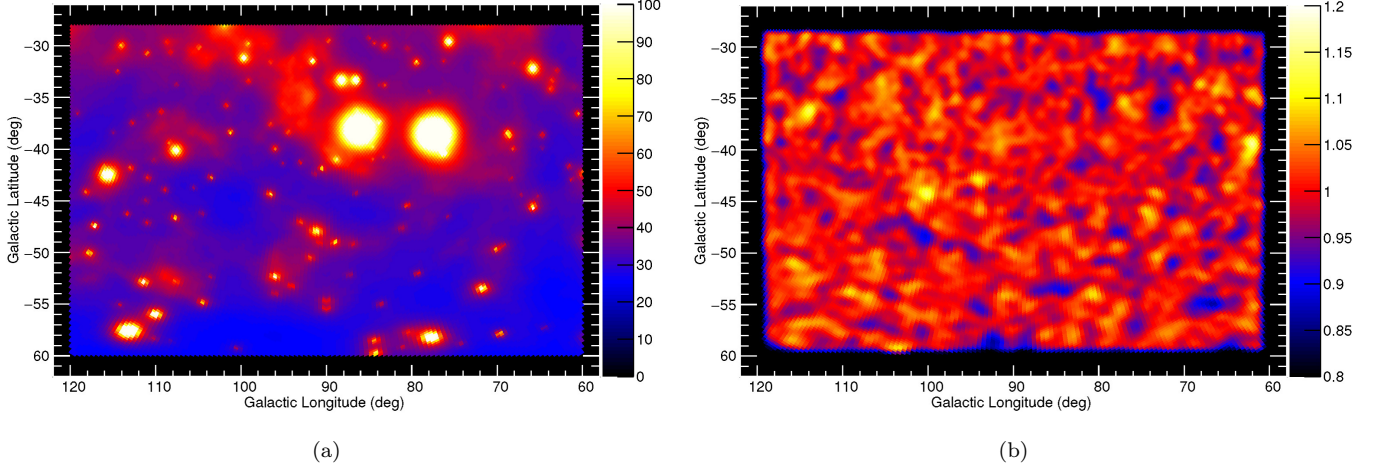


**Figure 5.** (a) The model count map. (b) The data/model ratio map. Both maps are obtained with a  $T_s$  correction (of 40 K) applied to the narrow H I template. Panel (b) is smoothed using a Gaussian kernel with  $\sigma = 60'$  for display.

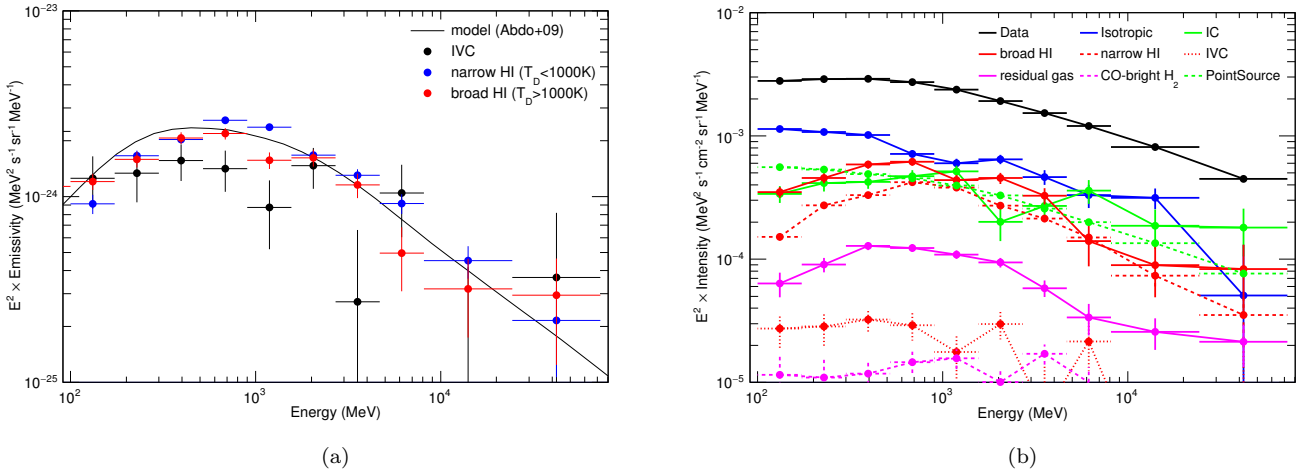


**Figure 6.** (a) The H I emissivity spectrum of IVC, narrow H I, and broad H I. (b) The spectrum of each component. Both panels are obtained by applying  $T_s$  corrections of 40 K to the narrow H I.

**Table 1.** Best-fit parameters, with 1-sigma statistical uncertainties, obtained by using gas templates with a  $T_s$  corrections of 40 K to the narrow H I.

Energy (GeV)	$C_{\text{H}1,1}$ (IVC)	$C_{\text{H}1,2}$ (narrow H I)	$C_{\text{H}1,3}$ (broad H I)	$C_{\text{CO}}$	$C_{\text{dust}}$	$C_{\text{IC}}$	$C_{\text{iso}}$
0.10–0.17	$0.97 \pm 0.30$	$0.70 \pm 0.08$	$0.93 \pm 0.09$	$0.58 \pm 0.25$	$0.18 \pm 0.04$	$0.70 \pm 0.11$	$1.18 \pm 0.05$
0.17–0.30	$0.68 \pm 0.21$	$0.84 \pm 0.05$	$0.81 \pm 0.08$	$0.37 \pm 0.15$	$0.19 \pm 0.03$	$0.89 \pm 0.13$	$1.20 \pm 0.06$
0.30–0.52	$0.66 \pm 0.15$	$0.86 \pm 0.04$	$0.88 \pm 0.06$	$0.34 \pm 0.10$	$0.22 \pm 0.02$	$0.99 \pm 0.12$	$1.25 \pm 0.06$
0.52–0.90	$0.60 \pm 0.15$	$1.10 \pm 0.04$	$0.93 \pm 0.07$	$0.42 \pm 0.09$	$0.22 \pm 0.02$	$1.26 \pm 0.15$	$1.04 \pm 0.07$
0.90–1.56	$0.41 \pm 0.17$	$1.12 \pm 0.04$	$0.74 \pm 0.08$	$0.51 \pm 0.09$	$0.22 \pm 0.02$	$1.67 \pm 0.18$	$1.06 \pm 0.09$
1.56–2.70	$0.86 \pm 0.21$	$0.98 \pm 0.06$	$0.95 \pm 0.10$	$0.40 \pm 0.11$	$0.24 \pm 0.02$	$0.79 \pm 0.24$	$1.44 \pm 0.13$
2.70–4.68	$0.22 \pm 0.32$	$1.07 \pm 0.08$	$0.95 \pm 0.14$	$0.93 \pm 0.18$	$0.20 \pm 0.03$	$1.34 \pm 0.34$	$1.19 \pm 0.16$
4.68–8.10	$1.29 \pm 0.54$	$1.13 \pm 0.14$	$0.61 \pm 0.23$	$0.82 \pm 0.27$	$0.18 \pm 0.05$	$2.26 \pm 0.49$	$0.92 \pm 0.20$
8.10–24.3	$0.13 \pm 0.77$	$0.97 \pm 0.19$	$0.69 \pm 0.31$	$0.46 \pm 0.35$	$0.24 \pm 0.07$	$1.66 \pm 0.58$	$1.06 \pm 0.20$
24.3–72.9	$1.80 \pm 2.21$	$1.06 \pm 0.54$	$1.44 \pm 0.84$	$0.00 \pm 0.03$	$0.45 \pm 0.17$	$2.68 \pm 1.12$	$0.27 \pm 0.43$

## 5. DISCUSSION

## 5.1. ISM properties

Assuming uniform CR intensity, we can evaluate the column density of each gas phase. We tabulated  $N_{\text{H}}$  integrated over the ROI in Table 2, where  $\int N_{\text{H}} d\Omega$  for broad H I is calculated assuming the optically thin case. The corresponding value of narrow H I is calculated with  $T_{\text{s}} = 40$  K. As described in Section 4.2, the emissivity ratio of narrow H I to broad H I is 1.13. We interpret this to mean that while the template map of broad H I represents optically thin H I distribution, that of narrow H I with  $T_{\text{s}} = 40$  K still underpredicts the true gas column density. Therefore we took this ratio into account in the calculation (i.e. true  $N_{\text{H}}$  of narrow H I is 13% larger.) We also calculated the integral of  $N_{\text{H}}$  for other gas phases using the average fitting coefficients given in Table 1. Although  $R/W_{\text{CO}}$  ratio has a large uncertainty (see Section 4.2), the effect on other gas phases is expected to be small since CO-bright  $\text{H}_2$  is the least significant component in our ROI (Table 2). To examine this expectation, we increased/decreased the  $R/W_{\text{CO}}$  ratio by a factor of 2 and repeated the analysis (construction of the residual gas template and  $\gamma$ -ray fit with it). While  $C_{\text{CO}}$  changed by  $\sim 20\%$ , the fit coefficients of other gas components were affected only at the 1% level.

Because the MBM 53-55 clouds and the Pegasus loop are located at similar distances from the solar system, and because most of the H I clouds are expected to coexist with the  $\text{H}_2$  clouds (because they are located at high Galactic latitudes), we can estimate the total mass of gas from  $N_{\text{H}}$  as

$$M = \mu m_{\text{H}} d^2 \int N_{\text{H}} d\Omega \quad , \quad (5)$$

where  $d$  is the distance to the cloud,  $m_{\text{H}}$  is the mass of the hydrogen atom, and  $\mu = 1.41$  is the mean atomic mass per H atom (Däppen 2000). From Equation (5),  $\int N_{\text{H}} d\Omega = 10^{22} \text{ cm}^{-2} \text{ deg}^2$  corresponds to  $\sim 740 M_{\odot}$  for  $d = 150 \text{ pc}$  (Welty et al. 1989). Therefore the mass of broad H I is estimated to be  $\sim 3 \times 10^4 M_{\odot}$ .

We interpret broad H I to be optically thin, narrow H I to be optically thick, and the residual gas to be CO-dark  $\text{H}_2$ . The values of  $\int N_{\text{H}} d\Omega$  for narrow H I is larger than that of the optically thin case by  $8.0 \times 10^{22} \text{ cm}^{-2} \text{ deg}^2$ , nearly equal to that of the residual gas. Therefore, the ratio of optical depth correction (to the H I column density) to CO-dark  $\text{H}_2$  is  $\sim 1$ . Because of the lack of information on  $T_{\text{s}}$ , this value has been used by several authors as one of possible cases in discussing the ISM properties (e.g. Planck Collaboration XXVIII 2015; Remy et al. 2018), and our result supports their assumption. The fraction of H I optical depth correction and CO-dark  $\text{H}_2$ , usually considered dark gas, is about 20% of the total gas column density. This agrees with the value obtained by Mizuno et al. (2016), which employed a different gas-modeling method.

We summarize the spatial distribution of dark gas in Figure 7. The left panel shows the distribution of H I optical depth correction, and the right panel shows that of CO-dark  $\text{H}_2$  in  $N_{\text{H}}$ . They show the different gas distribution and may help us understand how the gas evolves from thin H I to CO-bright  $\text{H}_2$  through two dark-gas phases (optically thick H I and CO-dark  $\text{H}_2$ ). The CO-dark  $\text{H}_2$  clearly traces the MBM 53-55 clouds and the Pegasus loop well, with similar peak  $N_{\text{H}}$  in two regions. On the other hand, H I optical depth correction (left panel) shows a similar but less structured distribution, with a larger amount of the gas in the Pegasus loop.

To examine the gas distributions in more detail, we defined two subregions, MBM 53-55 clouds and the Pegasus loop as  $l = 84^\circ$  to  $96^\circ$  and  $b = -44^\circ$  to  $-30^\circ$  and  $l = 99^\circ$  to  $109^\circ$  and  $b = -55^\circ$  to  $-35^\circ$ , respectively. Then we calculated the integral of the column density of each gas phase as summarized in Table 3. These results give a CO-dark  $\text{H}_2$  fraction, defined as the ratio of CO-dark  $\text{H}_2$  to total  $\text{H}_2$ , of 0.75 and more than 0.9 for MBM 53-55 clouds and the Pegasus loop, respectively. These values are larger than typical values (0.3–0.5) obtained by the Planck collaboration through dust emission observation in high latitude areas and that by Wolfire et al. (2010) through simulation. In other words, MBM 53-55 clouds and Pegasus loop were found to be rich in dark gas when normalized by total  $\text{H}_2$ .

A possible explanation of such a large CO-dark  $\text{H}_2$  fraction is due to the small gas column density that results in CO photodissociation. The value of  $N_{\text{H}}$  we found is a few  $\times 10^{21} \text{ cm}^{-2}$  (Figure 7). On the other hand, Wolfire et al. (2010) assumed clouds of larger column density ( $\geq 10^{22} \text{ cm}^{-2}$ ) and modeled the gas distribution using a photodissociation region code. We also note that Smith et al. (2014) predict that the CO-dark  $\text{H}_2$  fraction anticorrelates to molecular gas column density, and  $W_{\text{CO}}$  drops (the CO-dark  $\text{H}_2$  fraction increases) below the column density of a few  $\times 10^{21} \text{ cm}^{-2}$ . Indeed, Remy et al. (2018) reported that the CO-dark  $\text{H}_2$  fraction increases below the column density around this value in anticenter clouds.

In summary, the amounts of gas in H I optical depth correction and CO-dark  $\text{H}_2$  are similar in the Pegasus loop. The column density of  $\text{H}_2$  is above the threshold (a few  $\times 10^{21} \text{ cm}^{-2}$ ) only in thin and filamentary structures, and

hence, molecular gas is predominantly CO-dark. On the other hand, the dark gas in MBM 53-55 clouds is mostly CO-dark H<sub>2</sub> phase. The column density is above the threshold in large areas, and hence, CO-bright H<sub>2</sub> starts to form, and CO-dark H<sub>2</sub> fraction starts to decrease.

We remind that the discussion above depends on the assumption that broad H I and narrow H I correspond to the optically thin H I and thick H I, respectively. The assumption is based on our findings that (1) narrow H I gives  $\sim 1.5$  times larger emissivity than that of broad H I, and (2) there remains residual gas not accounted for by H I 21-cm lines. The discussion above also depends on our (simplified) optical depth correction to narrow H I using Equation (4). Systematic and large surveys of background radio sources will provide measurements of the H I optical depth and the ultimate answer of gas phases. Such large surveys, however, may not be feasible to cover all the nearby cloud complexes. Therefore, the analysis using  $\gamma$ -rays such as the one presented here is complementary and worthwhile.

**Table 2.** Integral for  $N_{\text{H}}$  of each gas phase

phase	$\int N_{\text{H}} d\Omega$ ( $10^{22}$ cm <sup>-2</sup> deg <sup>2</sup> )
broad H I	39.9
narrow H I	26.1 (8.0 over the thin-H I case)
IVC	2.8
residual gas	7.9
CO-bright H <sub>2</sub>	1.1

**Table 3.** Integral for  $N_{\text{H}}$  ( $10^{22}$  cm<sup>-2</sup> deg<sup>2</sup>) for two subregions

region	H I optical depth correction	CO-dark H <sub>2</sub>	CO-bright H <sub>2</sub>
MBM 53-55	0.7	2.3	0.8
Pegasus loop	1.8	1.9	0.1

## 5.2. CR properties

Finally, we discuss the H I emissivity spectrum and the inferred CR spectrum obtained in this study. Their properties can be evaluated in more detail with fewer gas templates. Therefore, we added the narrow H I (with the  $T_s$  correction) and broad H I templates and re-worked the  $\gamma$ -ray fitting. The obtained emissivity spectrum is summarized in Table 4 and Figure 8(a), together with those of other relevant studies (Casandjian 2015; Mizuno et al. 2020) and the emissivity model for the proton local interstellar spectrum (LIS) used in this study. Since we required the fit coefficient ratio of narrow H I to broad H I to be 1.0, we take the error of the latter ( $\sim 4\%$ ) as the systematic uncertainty of the emissivity. We also consider the LAT effective area uncertainty<sup>13</sup>; we assume the uncertainty to be 3% above 300 MeV, and 6% below 300 MeV where we used only PSF event types 2 and 3. By adding two types of systematics in quadrature, we obtained the overall uncertainty to be 5% and 7% above and below 300 MeV, respectively. Even if these systematic uncertainties are taken into account, our emissivity is lower than those of other studies. Also, while it agrees with the model above 1 GeV, we can recognize a small deviation at low energies. This suggests that there is a spectral break at around a few GeV that is stronger than that in the model. We note that Mizuno et al. (2016) found a hint of a similar deviation, although they could not give a firm conclusion since their analysis was limited above 300 MeV.

<sup>13</sup> [https://fermi.gsfc.nasa.gov/ssc/data/analysis/LAT\\_caveats.html](https://fermi.gsfc.nasa.gov/ssc/data/analysis/LAT_caveats.html)

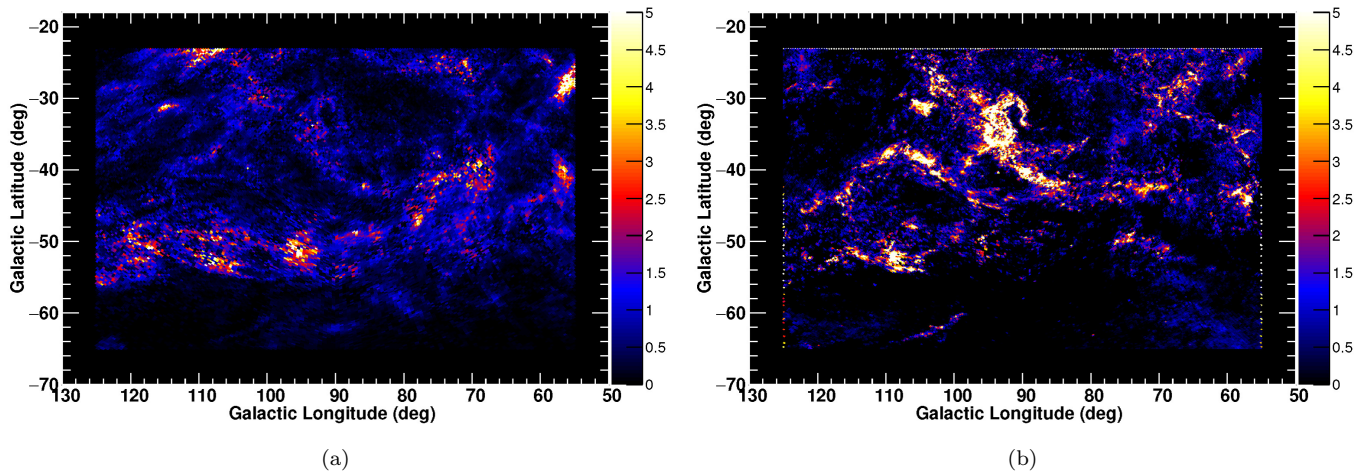


**Figure 7.** (a) The column density distribution of HI optical depth correction. (b) That of CO-dark H<sub>2</sub>. Both distributions are obtained by using the analysis with a  $T_s$  correction of 40 K to the narrow-HI template, and shown in  $10^{20}$  cm<sup>-2</sup>.

To investigate the inferred CR spectrum in more detail, we carried out simultaneous fitting of the proton and He CR observations and the  $\gamma$ -ray emissivity. We modeled the LIS and the solar-modulation effect using analytical formulae and then used a Markov chain Monte Carlo (MCMC) technique to constrain the model parameters; see Appendix C for details of the framework. The proton and He LIS models,  $J(p)$ , are expressed as a power law in momentum ( $p$ ) with two breaks:

$$J(p) \propto \left[ \left( \frac{p}{p_{\text{br1}}} \right)^{\alpha_1/\delta_1} + \left( \frac{p}{p_{\text{br1}}} \right)^{\alpha_2/\delta_1} \right]^{-\delta_1} \cdot \left[ 1 + \left( \frac{p}{p_{\text{br2}}} \right)^{\alpha_3/\delta_2} \right]^{-\delta_2}. \quad (6)$$

There,  $\alpha_1$  and  $\alpha_2$  are the indices in the high- and medium-energy ranges, respectively, and  $p_{\text{br1}}$  and  $\delta_1$  control the first (high-energy) spectral break. It is presumably due to a break in the interstellar diffusion coefficient (e.g., Ptuskin et al. 2006). The parameters  $p_{\text{br2}}$  and  $\delta_2$  control the second break, which represents an expected break due to ionization (e.g., Cummings et al. 2016), and  $\alpha_3$  is the difference in index over this break. Our formula is motivated by the work by Strong (2015), but it includes more parameters to represent the CR (and  $\gamma$ -ray) data over a broader energy range. It is still simple and hence allows us to fit to data within a reasonable computation time.

The  $\gamma$ -ray emissivity is calculated, based on the proton and He LIS models, using the AAFrag package (Kachelriess et al. 2019) and parameterizations in Kamae et al. (2006). We also add an electron/positron bremsstrahlung model by Orlando (2018), specifically their best propagation model called PDDE. In that work, constraints on the electron/positron LIS were obtained by fitting the CR direct measurements, the local synchrotron emission from radio to microwaves, and the local  $\gamma$ -rays emissivity.

In the CR and  $\gamma$ -ray modeling, we used nine proton datasets, including the AMS-02 data (from 2011 to 2013) and the Voyager 1 data (from 2012). We also used five He datasets, including the AMS-02 and Voyager 1 data from the same periods. All the CR data is retrieved from the Cosmic-Ray Data Base (Maurin et al. 2014). We used CR data other than AMS-02 and Voyager 1 to disentangle a possible degeneracy between the LIS shape and solar modulation. See Appendix C for details. We then obtained the parameters of the LIS model as summarized in Table 5. Other miscellaneous parameters are given in Appendix C (Table 8). The inferred CR spectrum and  $\gamma$ -ray emissivity spectrum are shown in Figure 8(b) and Figure 8(c), respectively. The scaling factor for  $\gamma$ -rays is  $1.07 \pm 0.03$  relative to the AMS-02 spectrum. Our LIS parameters are primarily constrained by CR data that have very small errors. The proton spectrum in 1–100 GeV mainly contributes to the  $\gamma$ -ray emissivity in the *Fermi*-LAT energy band, and our model emissivity spectrum reproduces the data well as shown in Figure 8(c). Our proton spectrum also agrees well with that of Boschini et al. (2020), which is based on CR data with a detailed calculation of the CR propagation in the heliosphere. This supports that our formula [Equation (6)] and force-field approximation well represent the LIS and the CR propagation in the heliosphere. The solar-modulation potential  $\Phi$  was found to be about 615 MV for AMS-02. For the high-energy spectral break, we obtained  $p_{\text{br1}} = 7.1 \pm 0.3$  GeV and  $\delta_1 = 0.07 \pm 0.01$ , confirming earlier claims

**Table 4.** The emissivity multiplied by  $E^2$ 

Energy	$E^2 \times \text{Emissivity}$
(GeV)	( $10^{-24} \text{ MeV}^2 \text{ s}^{-1} \text{ sr}^{-1} \text{ MeV}^{-1}$ )
0.10–0.17	$1.00 \pm 0.06$
0.17–0.30	$1.51 \pm 0.07$
0.30–0.52	$1.86 \pm 0.06$
0.52–0.90	$2.26 \pm 0.07$
0.90–1.56	$1.98 \pm 0.07$
1.56–2.70	$1.51 \pm 0.07$
2.70–4.68	$1.15 \pm 0.08$
4.68–8.10	$0.74 \pm 0.09$
8.10–24.3	$0.38 \pm 0.07$
24.3–72.9	$0.21 \pm 0.09$

of this spectral break from  $\gamma$ -ray data (e.g., [Strong 2015](#)) and CR data (e.g., [Ptuskin et al. 2006](#)). We note that our break energy is somewhat larger than that inferred from the CR data using the secondary to primary ratio (usually 3-5 GeV). This may be due to a spectral break in the CR injection spectrum in addition to a break in the interstellar diffusion coefficient (e.g., [Strong et al. 2007](#)). A detailed comparison of our LIS model to the primary and secondary CR data may clarify this issue and help us better understand the CR acceleration and propagation.

Recently, [Strong \(2015\)](#) and [Orlando \(2018\)](#) used the high-latitude  $\gamma$ -ray emissivity spectrum determined by [Casandjian \(2015\)](#) and obtained about 30% larger proton LIS than that measured at the Earth in the high-energy region. The discrepancy is larger than the uncertainties (at the 10% level) of their studies. If it is true, the CR spectrum at the Earth is not representative of the LIS. To examine this issue we compared proton LIS models in the GeV energy range based on  $\gamma$ -ray data (and CR data) in Figure 8(d). There, our LIS model is multiplied by 1.07 to take account of the scaling factor for  $\gamma$ -rays, and shown with the statistical error (3%) and systematic error (5%) summed in quadrature. As already shown in Figure 8(a), our emissivity is 10-15% lower than that by [Casandjian \(2015\)](#), giving the LIS model consistent with the AMS-02 spectrum within 10% in high energy where the solar modulation is irrelevant. Therefore, while the previous studies required the LIS larger than the PAMELA/AMS-02 spectra by  $\sim 30\%$ , our new study shows better agreement. We note that while [Casandjian \(2015\)](#) carried out detailed modeling of the high-latitude region and provided a very precise measurement of the  $\gamma$ -ray emissivity spectrum, it used Pass 7 data and assumed a uniform  $T_s$ , and hence the obtained spectrum might suffer from bias on the absolute value. Also, it samples a region of around  $\sim 1$  kpc and hence may deviate from the prediction based on the CR spectrum directly measured at the Earth, while the MBM 53-55 clouds and the Pegasus loop are very close to us. Of course, our result is based on a particular region in the sky, and a systematic study of local regions is crucial to settle the issue. Such a systematic study is also crucial to investigate a possible local variation of the CR spectrum.

**Table 5.** Parameters of the LIS obtained by fitting the CR and  $\gamma$ -ray data

parameter	proton	He
normalization	$26.20 \pm 0.10$	$1.41 \pm 0.01$
$\alpha_1$	$2.86 \pm 0.01$	$2.76 \pm 0.01$
$\alpha_2$		$2.57 \pm 0.02$
$\alpha_3$	$-3.25 \pm 0.05$	$-2.73 \pm 0.08$
$R_{br1}$ (GV)	$7.08 \pm 0.31$	
$\delta_1$		$0.07 \pm 0.01$
$R_{br2}$ (GV)	$0.524 \pm 0.015$	$1.314 \pm 0.061$
$\delta_2$	$1.91 \pm 0.07$	$0.82 \pm 0.07$

NOTE— Normalization is the flux [ $\text{c s}^{-1} \text{m}^{-2} \text{sr}^{-1} (\text{GeV}/\text{n})^{-1}$ ] at  $p = 10$  GeV. CR protons and He are assumed to share the value of the high-energy spectral break in rigidity. Therefore breaks in rigidity ( $R_{br}$ ) are given instead of breaks in momentum.

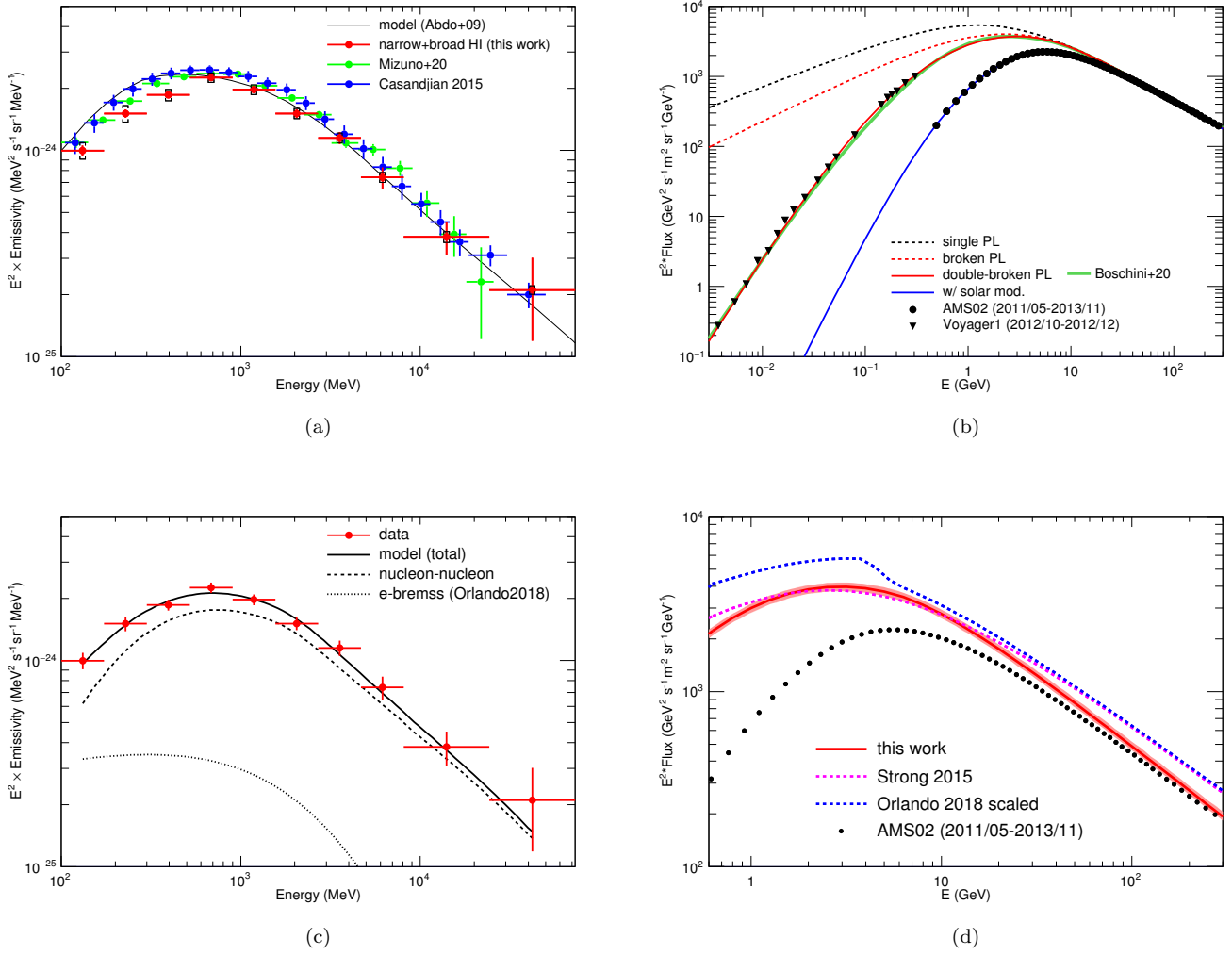


**Figure 8.** (a) The H I emissivity spectrum obtained in this study (red points) compared with the model curve and the results of relevant studies from *Fermi*-LAT (Casandjian 2015; Mizuno et al. 2020). Square brackets represent the systematic errors. The emissivity model adopted in this analysis is also shown as a solid black line. (b) The CR proton LIS obtained by fitting the CR and  $\gamma$ -ray data. The LIS and the spectrum at the Earth are shown by the solid red and blue lines, respectively. For reference, a spectrum without break and one with only the high-energy break are shown by the dotted black and red lines, respectively. The spectrum obtained by Boschini et al. (2020) is shown by the green line for comparison. (c) The emissivity model spectrum obtained by fitting the CR and  $\gamma$ -ray data. The data is shown with the statistical and systematic errors summed in quadrature. Contributions of hadronic interaction and electron bremsstrahlung are indicated. See Appendix C for details of the model calculations. (d) A comparison of LIS models based on  $\gamma$ -ray emissivities (this work, that of Strong (2015), and that of Orlando (2018)) in GeV energy range. The AMS-02 data is also shown. Our LIS is multiplied by 1.07 to include the scaling factor for  $\gamma$ -rays. The LIS of Strong (2015) has been obtained by fitting an analytical formula to the emissivity by Casandjian (2015), and that of Orlando (2018) has been obtained by scaling a CR propagation model called PDDE to fit the same emissivity spectrum. The uncertainty of our LIS is shown by a light-red shaded band. Those for Strong (2015) and Orlando (2018) are not presented for clarity.

## 6. SUMMARY

We carried out a detailed study of the ISM and CRs using the *Fermi*-LAT data in the 0.3-72.9 GeV energy range at Galactic longitudes from  $60^\circ$  to  $120^\circ$  and Galactic latitudes from  $-60^\circ$  to  $-28^\circ$ . This region encompasses the MBM 53-55 clouds and the Pegasus loop. We improved the ISM gas modeling over our previous work by using the Gaussian decomposition of the 21-cm line emission. We succeeded in distinguishing optically thin H I, optically thick H I, and CO-dark H<sub>2</sub> gas phases. We found the fractions of H I optical depth correction and of CO-dark H<sub>2</sub> to be nearly equal, and we found the fraction of dark gas to be about 20% of the total gas column density. The CO-dark H<sub>2</sub> fraction is higher in the Pegasus loop than in the MBM 53-55 clouds, likely due to the CO photodissociation. While the H I emissivity spectrum agrees with the adopted model of the LIS above 1 GeV, there is a small deviation below a few hundreds of MeV. We fitted the CR spectra measured at/near the Earth and the measured  $\gamma$ -ray spectrum simultaneously, and we obtained a spectral break in the proton LIS at  $\sim 7$  GeV. Our new emissivity spectrum relaxes the tension with the CR spectra directly measured at the Earth, and agrees with the AMS-02 spectrum within 10%.

1 The *Fermi* LAT Collaboration acknowledges generous ongoing support from a number of agencies and institutes that  
 2 have supported both the development and the operation of the LAT as well as scientific data analysis. These include the  
 3 National Aeronautics and Space Administration and the Department of Energy in the United States, the Commissariat  
 4 à l’Energie Atomique and the Centre National de la Recherche Scientifique / Institut National de Physique Nucléaire  
 5 et de Physique des Particules in France, the Agenzia Spaziale Italiana and the Istituto Nazionale di Fisica Nucleare  
 6 in Italy, the Ministry of Education, Culture, Sports, Science and Technology (MEXT) and High Energy Accelerator  
 7 Research Organization (KEK) in Japan, and the K. A. Wallenberg Foundation, the Swedish Research Council and the  
 8 Swedish National Space Board in Sweden.

9 Additional support for science analysis during the operations phase is gratefully acknowledged from the Istituto  
 10 Nazionale di Astrofisica in Italy and the Centre National d’Études Spatiales in France. This work performed in part  
 11 under DOE Contract DE-AC02-76SF00515.

12 This work was partially supported by JSPS Grants-in-Aid for Scientific Research (KAKENHI) grant No. 17H02866  
 13 (T.M.) and by Core of Research for the Energetic Universe at Hiroshima University. E.O. acknowledges the ASI-INAF  
 14 agreement n. 2017-14-H.0 and the NASA Grant No. 80NSSC22K0495 GALPROP development is partially supported  
 15 through NASA grant NNX17AB48G.

*Software:* emcee (Foreman-Mackey et al. 2013), Fermitools (v2.0.0; Fermi Science Support Development Team 2019), AAfrag (Kachelriess et al. 2019)

## APPENDIX

## A. TREATMENT OF THE INFRARED SOURCES

In the *Planck* dust-model maps from Data Release 1, we identified several regions with high  $T_d$ , indicating localized heating by stars. We refilled these areas in the  $R$ ,  $\tau_{353}$ , and  $T_d$  maps with the average of the peripheral pixels: values in a circular region of radius  $r_1$  are filled with the average of the pixels in an annulus with inner radius  $r_1$  and outer radius  $r_2$ . For each region, the central position  $(l, b)$ ,  $r_1$ , and  $r_2$  are summarized in Table 5. Since the area of high  $T_d$  located near 3C 454.3 is large, we used a larger radius for it. We found that the *Planck* Data Release 2 maps are less affected by infrared sources, and we had to mask only RAFGL 3068.

## B. IC MODEL

We employed recent work by Porter et al. (2017) to construct the IC model template. They employed 3D spatial models for the CR source distribution and the ISRF. They considered three different spatial distributions for the CR sources (differentiated by the ratio of the smooth-disk component to the spiral-arm component) and three ISRFs. The three CR source distributions are labeled SA0, SA50, and SA100; SA0 corresponds to a 100% (2D) disk, and SA100 corresponds to a 100% spiral-arm contribution. For the ISRF, they used a standard 2D ISRF (labeled Std) and two 3D ISRFs (labeled R12 and F98). We tested all nine IC models and a model used by Mizuno et al. (2016) (labeled 54\_77Xvarh7S) against the  $\gamma$ -ray data using our baseline gas model. We found that the SA0 models give a better

**Table 6.** Infrared sources excised and interpolated across in the *Planck* dust maps

Position		$r_1$	$r_2$	Object name
$l$ (deg)	$b$ (deg)	(deg)	(deg)	
79.61	-30.25	0.12	0.15	
82.85	-50.65	0.12	0.15	
83.10	-45.46	0.12	0.15	
86.30	-38.20	0.60	0.65	3C 454.3 (Active galactic nucleus)
87.46	-29.73	0.12	0.15	NGC 7339 (Radio galaxy)
87.57	-39.12	0.12	0.15	
93.53	-40.35	0.12	0.15	RAFGL 3068 (Variable star)
93.91	-40.47	0.12	0.15	NGC 7625 (Interacting galaxies)
97.29	-32.52	0.12	0.15	IC 5298 (Seyfert2 galaxy)
98.88	-36.55	0.12	0.15	NGC 7678 (Active galactic nucleus)
104.26	-40.58	0.12	0.15	
104.46	-40.14	0.12	0.15	
111.37	-36.00	0.12	0.15	

fit than the others in terms of log-likelihoods, and that the difference among the three ISRF is minor. We therefore decided to use the SA0-Std model in this study.

### C. CR AND GAMMA-RAY FITTING FRAMEWORK

To investigate the interstellar CR spectrum in detail, we have developed a framework that simultaneously fits the CR and  $\gamma$ -ray data. It models the LIS and the solar-modulation effect using analytical formulae, and it uses a Markov chain Monte Carlo (MCMC) technique to constrain the model parameters. Specifically, we use the `emcee`<sup>14</sup> (Foreman-Mackey et al. 2013) python package that implements the affine-invariant ensemble sampler (Goodman & Weare 2010). Solar modulation is taken into account using a force-field approximation (Gleeson & Axform 1968), and the LIS is modeled as a power law of momentum with two breaks [see Equation (6)]. In the  $\gamma$ -ray spectrum calculation, we take account of p-p, p-He, He-p, and He-He interactions individually using the `AAfrag` package (Kachelriess et al. 2019) and parameterizations in Kamae et al. (2006). Specifically, we adopt the calculations using the `AAfrag` package above 10 GeV/n and use the parameterizations by Kamae et al. (2006) below that energy. For the p-p interaction, we use the non-diffractive component of Kamae et al. (2006), since it smoothly connects to the `AAfrag` calculation. For the p-He and He-p interactions, we use the p-p interaction model by Kamae et al. (2006) multiplied by a factor of 4 to connect it smoothly to the `AAfrag` calculation. For He-He interaction, we adopt a scale factor of 14. The contribution of heavier nuclei to the  $\gamma$ -ray spectrum is small, and we use an enhancement factor based on the formalism of Kachelriess et al. (2014) to scale the flux up to account for all other elements in the CRs and the interstellar gas. We adopt the spectra from Honda et al. (2004) and the abundances in the interstellar medium from Meyer (1985) for the heavier nuclei in the CRs and the ISM gas, respectively. We also add an electron/positron bremsstrahlung model by Orlando (2018), specifically their best propagation model called PDDE. In that work, constraints on the electron/positron LIS were obtained by fitting the CR direct measurements (Voyager 1 and AMS-02), the local synchrotron emission from radio to microwaves (radio surveys and *Planck* data), and the local  $\gamma$ -rays emissivity by Casandjian (2015). This method allows to obtain a consistent electron/positron LIS independent from assumptions on the solar modulation.

The framework reads the AMS-02 data (taken in 2011-2013), the Voyager 1 data (taken in 2012), and the *Fermi*-LAT  $\gamma$ -ray data. To disentangle a possible degeneracy between the shape of the LIS and solar modulation, we can use other CR data. All the CR data is retrieved from the Cosmic-Ray Data Base (Maurin et al. 2014), but datapoints above

<sup>14</sup> <https://emcee.readthedocs.io/en/stable/>

300 GeV are not used in the fitting. The CR data and  $\gamma$ -ray data share the same spectral shape of the LIS, but the normalizations (relative to that of AMS-02) are allowed to vary to account for possible systematic uncertainties. The solar-modulation potential  $\phi$  is also set free for each CR dataset, and it is set to be 0 V for Voyager 1 data. The proton and He data of the same experiment and observational period share the common value of  $\phi$ . Since the high-energy break is presumably due to a break in the interstellar diffusion coefficient, CR protons and He ions share  $\delta_1$  and a common value of rigidity for  $p_{\text{br1}}$ .  $\alpha_2$  is also common among them. We also limit parameter ranges as summarized in Table 7. Except for Voyager 1,  $\phi$  is limited within  $\pm 15\%$  of the value calculated based on [Usoskin \(2017\)](#) and the observational period. For prior probabilities, we adopt the Gaussian distribution for LIS normalizations (relative to that of AMS-02); the standard deviations are 0.05 and 0.1 for CR data and  $\gamma$ -ray emissivity, respectively. We adopt the flat distribution for other parameters. The likelihood is calculated assuming the Gaussian distribution for each CR/ $\gamma$ -ray datapoints (statistical error and systematic error are summed in quadrature). The framework then runs the MCMC fitting to constrain the LIS parameters and  $\phi$ . The list of datasets used for this study and obtained values of  $\phi$  and LIS normalization are summarized in Table 8.

**Table 7.** Parameters ranges

parameter	range
proton normalization	22.5-27.5
$\alpha_1$	2.7-3.0
$\alpha_2$	2.2-2.7
$\alpha_3$	< 0
$R_{\text{br1}}$ (GV)	2-10
$R_{\text{br2}}$ (GV)	0.1-2
$\delta_1$	0.05-2
$\delta_2$	0.05-2
$\phi$	$(0.85 - 1.15) \times \phi_0$

NOTE— Normalization is the flux [ $\text{c s}^{-1} \text{ m}^{-2} \text{ sr}^{-1} (\text{GeV/n})^{-1}$ ] at  $p = 10$  GeV. CR protons and He are assumed to share the value of the high-energy spectral break in rigidity. Therefore breaks in rigidity ( $R_{\text{br}}$ ) are given instead of breaks in momentum.  $\phi_0$  is the reference value of  $\phi$  calculated based on [Usoskin \(2017\)](#) and the observational period.

**Table 8.** Datasets and their  $\phi$  and relative normalization

experiment	$\phi$ (GV)	relative normalization
AMS-02, 2011/05-2013/11 (proton, He)	$614.7 \pm 4.7$	1
Voyager 1, 2012/10-2012/12 (proton, He)	0	1
AMS-01, 1998/06 (proton)	$472^a$	$1.028 \pm 0.009$
BESS-PolarI, 2004/12 (proton, He)	$668.4 \pm 4.4$	$1.012 \pm 0.004$
BESS-PolarII, 2007/12-2008/01 (proton, He)	$386.5 \pm 3.7$	$0.959 \pm 0.004$
BESS-TeV, 2002/08 (proton, He)	$1055.0 \pm 7.5$	$0.986 \pm 0.004$
PAMELA, 2006/07 (proton)	$504.1 \pm 5.0$	1
PAMELA, 2008/03-2008/04 (proton)	$404.6 \pm 4.8$	1
PAMELA, 2010/01 (proton)	$293.7 \pm 5.4$	1
$\gamma$ -ray emissivity, this work	0	$1.066 \pm 0.025$

NOTE— The value of  $\phi$  is set to 0 for Voyager 1 data. LIS normalizations are scaled to that of AMS-02 and allowed to vary. Some experiments do not have enough high-energy datapoints to constrain the normalization; in such a case, the relative normalization is fixed to 1.

<sup>a</sup>Although the best-fit value of  $\phi$  is at the parameter limit, the spectrum is represented by the model well.

## REFERENCES

- Abdo, A. A., Ackermann, M., Ajello, M., et al. 2009a, *Astropart. Phys.*, 32, 193
- Abdo, A. A., Ackermann, M., Ajello, M., et al. 2009b, *ApJ*, 703, 1249
- Abdo, A. A., Ackermann, M., Ajello, M., et al. 2010, *ApJ*, 710, 133
- Abdollahi, S., Acero, F., Ackermann, M., et al. 2020, *ApJS*, 247, 33
- Ackermann, M., Ajello, M., Baldini, L., et al. 2011, *ApJ*, 726, 81
- Ackermann, M., Ajello, M., Atwood, W. B., et al. 2012a, *ApJ*, 750, 3
- Ackermann, M., Ajello, M., Allafort, A., et al. 2012b, *ApJ*, 755, 22
- Atwood, W. B., Abdo, A. A., Ackermann, M., et al. 2009, *ApJ*, 697, 1071
- Atwood, W. B., Albert, L., Baldini, L., et al. 2013, *arXiv:1303.3514*
- Boschini, M. J., Torre, S. D., Gervasi, M., et al. 2020, *ApJS*, 250, 27
- Bruel, P., Burnett, T. H., Digel, S. W., et al. 2018, *arXiv:1810.11394*
- Casandjian, J.-M. 2015, *ApJ*, 806, 240
- Cummings, A. C., Stone, E. C., Heikkila, B. C., et al., 2016, *ApJ*, 831, 18
- Dame, T. M., Hartmann, D., & Thaddeus, P. 2001, *ApJ*, 547, 792
- Dame, T. M. 2011, *arXiv:1101.1499*
- Däppen, W. 2000, in *Allen's Astrophysical Quantities*, ed. A. N. Cox (4th ed.; New York: Springer), 27
- Dickey, J. M., & Lockman, F. J. 1990, *ARA&A*, 28, 215
- Ferriere, K. M. 2001, *Rev. Mod. Phys.*, 73, 1031
- Fukui, Y., Okamoto, R., Kaji, et al. 2014, *ApJ*, 796, 59
- Foreman-Mackey, D., W. Hogg, D., Lang, D., et al. 2013, *PASP*, 125, 306
- Fukui, Y., Torii, K., Onishi, T., et al. 2015, *ApJ*, 798, 6
- Fukui, Y., Koga, M., Maruyama, S., et al. 2021, *PASJ73*, S117
- Górski, K. M., Hivon, E., Banday, A. J., et al. 2005, *ApJ*, 622, 759
- Gleeson, J. J., & Axford, W. I. 1968, *ApJ*, 154, 1011
- Goodman, J., & Weare, J. 2010, *Comm. App Math. Comp. Sci.*, 5, 65
- Grenier, I. A., Casandjian, J.-M., & Terrier, R. 2005, *Science*, 307, 1292
- Grenier, I. A., Black, J. H., & Strong, A. W. 2015, *ARA&A*, 53, 199
- Ferriere, K. M. 2001, *Rev. Mod. Phys.*, 73, 1031
- Hayashi, K., Mizuno, T., Fukui, Y., et al. 2019, *ApJ*, 884, 130
- Honda, M., Kajita, T., Kasahara, K. et al. 2004, *PhRvD*, 70, 043008
- HI4PI Collaboration 2016, *A&A*, 594, 116
- Kachelriess, M., Moskalenko, I. V., & Ostapchenko, S. 2014, *ApJ*, 789, 136
- Kachelriess, M., Moskalenko, I. V., & Ostapchenko, S. 2019, *Computer Physics Communications*, 245, 106846
- Kalberla, P.M. W., & Kerp, J. 2009, *ARA&A*, 47, 27
- Kalberla, P.M. W., & Haud, U. 2018, *A&A*, 619, 58
- Kalberla, P.M. W., Kerp, J., & Haud, U. 2020, *A&A*, 639, 26
- Kamae, T., Karlsson, N., Mizuno, T., et al. 2006, *ApJ*, 647, 692
- Mattox, J. R., Bertsch, D. L., Chiang, J., et al. 1996, *ApJ*, 461, 396
- Maurin, D., Melot, F., & Taillet, R. 2014, *A&A*, 569, 32
- Meyer, J. P. 1985, *ApJS*, 57, 173
- Mizuno, T., Abdollahi, S., Fukui, Y., et al. 2016, *ApJ*, 833, 278
- Mizuno, T., Abdollahi, S., Fukui, Y., et al. 2020, *ApJ*, 890, 120
- Moskalenko, I. V., Porter, T., Strong W. 2006, *ApJL*, 640, 155
- Murray, C. M., Peek, J.E. G., Lee, M.-Y., et al. 2018, *ApJ*, 862, 131
- Orlando, E. 2018, *MNRAS*, 475, 2724
- Planck Collaboration XIX 2011, *A&A*, 536, 19
- Planck Collaboration XI 2014, *A&A*, 571, 11
- Planck Collaboration XXVIII 2015, *A&A*, 582, 31
- Porter, T. A., Jóhannesson, G., Moskalenko, I. V. 2017, *ApJ*, 846, 23
- Ptuskin, V. S., Moskalenko, I. V., Jones, F. C., et al. 2006, *ApJ*, 642, 902
- Reach, W. T., Bon-Chul, K., & Carl, H. 1994, *ApJ*, 429, 672
- Remy, Q., Grenier, I. A., Marshall, D. J., & Casandjian, J. M. 2017, *A&A*, 601, 78
- Remy, Q., Grenier, I. A., Marshall, D. J., & Casandjian, J. M. 2018, *A&A*, 611, 51
- Schlegel, D. J., Finkbeiner, D. P., & Davis, M. 1998, *ApJ*, 500, 525
- Smith, R. J., Glover, S. C. O., Clark, P. C. 2004, *MNRAS*441, 1628
- Strong, A. W., & Moskalenko, I. 1998, *ApJ*, 509, 212
- Strong, A. W., Moskalenko, I.V., & Ptuskin, V. S. 2007, *ARA&A*, 57, 285
- Strong, A. W. 2015, *Proc. ICRC*, (The Hague, The Netherlands), 34, 506

Usoskin, I. G., Agnieszka, G., Kovaltsov, G. A., et al. 2017,  
J. Geophys. Res., 122, 3875  
Wakker, B. P. 2001, ApJS, 136, 463  
Welty, D. E., Hobbs, L. M., & Penprase, B. E. 1989, ApJ,  
346, 232

Wolfire, M. G., Hollenbach, D., & McKee, C. F. 2010, ApJ,  
716, 1191  
Yamamoto, H., Kawamura, A., Tachihara, K., et al. 2006,  
ApJ, 642, 307